







Robust Multiscale Spectral–Spatial Regularized Sparse Unmixing for Hyperspectral Imagery

Ke Wang , Lei Zhong , Jiajun Zheng , Shaoquan Zhang , *Member, IEEE*, Fan Li , Chengzhi Deng ,
Jingjing Cao , and Dingli Su 

Abstract—With the aid of endmember spectral libraries, sparse unmixing plays a critical role in interpreting hyperspectral remote sensing data. Integrating spatial clues from hyperspectral data into sparse unmixing frameworks is pivotal for enhancing unmixing capabilities. As such, extracting and harnessing spatial signatures from imagery has emerged as a prevalent tactic to optimize unmixing. In real-world scenarios, hyperspectral images are susceptible to noise, which poses great challenges to the separability of ground objects. As a result, most sparse unmixing models are ill-equipped to handle this issue properly, facing risks of failure. To tackle this challenge, we proposed a sparse unmixing technique with robust multiscale spectral–spatial regularization (RMSR). In the proposed RMSR model, an abundance estimation error reduction regularizer and a spectral–spatial weighted sparse regularizer are consolidated into a unified framework, which excavates the spatial information of the image from multiple perspectives. Specifically, in the first part, the abundance estimation error is defined as the difference between the precomputed abundance maps at the superpixel level and the expected abundances calculated from the

original data. Then, the $\ell_{2,1}$ norm is applied to it as a regularization term, which enhances the robustness of the model against image noise and outliers. In the second part, image level spectral weighting coefficients and local spatial weighting terms are leveraged to individually enhance the sparsity of the abundance maps and their piecewise smoothness. The experimental results reveal the algorithm’s considerable capabilities in noise immunity and improved unmixing abilities.

Index Terms—Abundance estimation error, multiscale, sparse hyperspectral unmixing, spatial information, spatial regularization.

I. INTRODUCTION

HYPERSPECTRAL remote sensing uniquely combines spectral and spatial data, revealing detailed spectral signatures of surface materials absent in traditional broadband imagery [1]. This fusion of spectroscopic and imaging capabilities enables fine-grained identification and characterization of ground components, which is critical for advanced analysis [2], [3]. Hyperspectral remote sensing has found diverse applications across domains, including mineral exploration [4], crop analytics [5], ecological surveying [6], seafloor mapping [7], and defense reconnaissance [8], [9]. Hyperspectral sensors often have inherent resolution limitations that lead to mixed pixels in the imagery, where the measured spectrum represents an aggregate of multiple ground components [10]. The ubiquity of these mixed pixels hinders detailed analysis and practical use cases of hyperspectral data by obscuring the pure spectral signatures of interest [11]. Spectral unmixing provides a useful approach for tackling mixed pixels in hyperspectral data [12]. It seeks to unmix the mixed spectrum of each pixel into its pure endmember spectra and quantify the fractional abundance of each endmember in that pixel [13].

With its simple formulation and intuitive interpretability, the linear mixture model (LMM) has gained popularity in hyperspectral imaging analysis [14]. Under LMM, the composite spectrum of a mixed pixel is modeled as a linear summation of the constituent endmember signatures present within that pixel [15]. Unsupervised spectral unmixing techniques have emerged as a result of advancements built upon the LMM. These techniques encompass geometric-based [16], [17], [18], statistical-based [19], [20], [21], and nonnegative matrix factorization (NMF) [22], [23], [24] methods. A potential drawback of these pure data-driven unmixing approaches is that they may extract endmembers that lack physical meaning from

Manuscript received 27 September 2023; revised 4 November 2023; accepted 16 November 2023. Date of publication 28 November 2023; date of current version 14 December 2023. This work was supported in part by the National Natural Science Foundation of China under Grant T2225019, Grant 62361042, Grant 42361061, and Grant 42201353, in part by the Jiangxi Provincial Natural Science Foundation under Grant 20232BAB202039, Grant 20224ACB202002, and Grant 20224BAB202007, in part by the Training Program for Academic and Technical Leaders of Jiangxi Province under Grant 20225BCJ23019, in part by the Chinese Ministry of Education Chunhui Plan Collaborative Research Project under Grant 202201108, in part by the Guangdong Provincial Department of Housing and Urban-Rural Development Science and Technology Plan Project under Grant 2021-K1-140626, in part by the Science and Technology Project of Guangzhou Construction Company Ltd., under Grant [2021]-KJ019 and Grant [2021]-KJ059, and in part by the Research Project of China Construction Enterprise Management Association under Grant 2023-B-033. (*Corresponding authors: Shaoquan Zhang; Fan Li.*)

Ke Wang is with the Hubei Key Laboratory of Intelligent Geo-Information Processing, School of Computer Science, China University of Geosciences, Wuhan 430078, China (e-mail: 2417621285@qq.com).

Lei Zhong is with the Third Surveying and Mapping Institute of Hunan Province, Changsha 410029, China (e-mail: 24547388@qq.com).

Jiajun Zheng, Shaoquan Zhang, and Chengzhi Deng are with the Jiangxi Province Key Laboratory of Water Information Cooperative Sensing and Intelligent Processing, School of Information Engineering, Nanchang Institute of Technology, Nanchang 330099, China (e-mail: 2718706166@qq.com; zhangshaoquan1@163.com; dengcz@nit.edu.cn).

Fan Li is with the Hubei Key Laboratory of Intelligent Geo-Information Processing, School of Computer Science, China University of Geosciences, Wuhan 430078, China, and also with the Jiangxi Province Key Laboratory of Water Information Cooperative Sensing and Intelligent Processing, School of Information Engineering, Nanchang Institute of Technology, Nanchang 330099, China (e-mail: fairylifan@163.com).

Jingjing Cao is with the College of Computer Sciences, Guangdong Polytechnic Normal University, Guangzhou 510665, China (e-mail: caojj@gpnu.edu.cn).

Dingli Su is with the Guangzhou Institute of Building Science Group Company Ltd., Guangzhou 510440, China (e-mail: sudingli@mail2.sysu.edu.cn).

Digital Object Identifier 10.1109/JSTARS.2023.3337130

the scene [25], [26]. By deriving endmember signatures solely from the available mixed hyperspectral pixels, the extracted spectral profiles may not correspond to actual materials present in the image. This can lead to virtual endmembers that are mathematical abstractions without real-world counterparts [27]. Driven by growing spectral libraries and progress in sparse modeling [28], [29], sparse unmixing has become a prevalent semisupervised technique for hyperspectral analysis [30]. It aims to select the most representative endmember signatures from a large preexisting library to accurately model each mixed pixel [31]. By leveraging sparsity to reconstruct mixed spectra, this approach provides a promising solution to limitations of previous methods.

In reality, each mixed pixel is composed of only a small subset of endmembers from the full spectral library, which is sparse relative to the full spectral library containing numerous endmember signatures [32]. This intrinsic sparsity induces sparse abundance vectors during unmixing. Capitalizing on the intrinsic sparsity, some sparse unmixing techniques dedicate efforts to promoting and leveraging the inherent sparse structure within the estimated abundance matrix. For instance, the ℓ_1 norm readily quantifies sparsity levels of the abundances [30]. Meanwhile, the $\ell_{2,1}$ norm enforces joint sparsity to yield row-sparse solutions that align with the endmembers present [33]. In addition, nonconvex regularizers, such as ℓ_p for $0 \leq p < 1$, strengthen sparse induction during optimization [34]. By incorporating such sparsity-driving constraints and priors, these methods produce abundances with enhanced sparsity consistent with the true endmember composition. Moreover, weighted sparse unmixing approaches represent the prevailing techniques that induce markedly elevated sparsity in estimated abundances through diverse weighting schemes [35], [36]. Examples include double reweighted sparse unmixing (DRSU) that impose twin weighting factors [37], as well as dual weighted low-rank sparse unmixing that concurrently leverage both weighted and low-rank priors [38]. By integrating multiple complementary sparsity-promoting regularizers in a joint optimization framework, these weighted sparse unmixing methods can effectively tease out the intrinsic sparse structures within hyperspectral data.

Incorporating the abundant spatial context of hyperspectral imagery into conventional sparse unmixing frameworks, as substantiated by prior arts, allows more precise direction of abundance estimation and holds promise for performance enhancement [39], [40], [41], [42]. To illustrate, the renowned total variation (TV) regularization is applied to enhance the spatial continuity of estimated abundance maps [43], [44]. Superpixel segmentation methods are adopted to construct more precise adaptive spatial contexts [45]. Sparse graph regularization effectively encodes the interrelatedness between data points by constructing a sparse graph structure of nodes, retaining important structural information [46], [47], [48]. The NLSU method retains the nonlocal spatial structures in the abundances by leveraging the nonlocal similarity existing in the image [49]. The multiscale spatial regularization unmixing method is proposed, which captures spatial and spectral contextual information through multiscale domain transformation techniques to achieve fast unmixing [50]. Moreover, spectral and spatial weighting terms

are incorporated into the ℓ_1 unmixing model to strengthen spatial coherency [51].

Nonetheless, the preceding approaches struggle to attain adequate unmixing fidelity under scenarios where hyperspectral imagery is polluted by excessive noise contamination. To remedy this predicament, a robust self-supervised deep unmixing network model has been introduced [52]. By exploiting deep autoencoders, it curtails the detrimental impact of Gaussian and sparse noise on unmixing performance, thereby boosting unmixing capabilities. To mitigate the effects of noise, a robust sparse unmixing approach with dual spatial weighting based on superpixels has been presented [53]. By employing dual spatial weighting coefficients, it successfully relieves the interference of noise with unmixing and attains commendable performance. The SSNPMMF unmixing model is proposed, which adopts a spatial graph regularization approach to smooth the hyperspectral image for reducing noise interference [54].

Motivated by filtering-based image denoising approaches, we have introduced a novel robust multiscale spectral–spatial regularization technique for sparse hyperspectral unmixing (RMSR). This is aimed at enhancing the unmixing performance on heavily noise-contaminated hyperspectral imagery. The proposed RMSR unmixing model incorporates abundance estimation error mitigation and spatial–spectral weighted sparse unmixing into a cohesive framework that extracts the spatial details of the imagery through various approaches. To begin with, the hyperspectral image is partitioned into superpixels by leveraging the renowned simple linear iterative clustering (SLIC) algorithm [45]. Subsequently, the pixels enclosed in each superpixel are averaged, and the superpixel is endowed with the resulting new mean value, thereby reconstituting a new hyperspectral image. This procedure bears similarity to mean filtering, thereby capable of substantially mitigating noise. Subsequently, optimization algorithms are employed to deduce the abundance details at the superpixel level from the reconstructed hyperspectral image. The deviation between it and the anticipated abundance of the raw data is leveraged to configure a regularization constituent founded on the $\ell_{2,1}$ norm, instead of acting as an outright abundance solution. This regularization term is integrated into the unmixing model to induce the nonzero row vectors of abundances tend to the desired endmembers. Moreover, the spectrally weighted coefficients grounded on the holistic scale of the imagery and the spatially weighted coefficients stemming from the 8-adjacency scale are amalgamated into the sparseness regularization constituted on the ℓ_1 norm, analogous to the work in [51], in order to augment the sparseness and piecewise continuity of the abundance maps, respectively. The cardinal contributions of this undertaking can be encapsulated as ensues.

- 1) A new regularization term is introduced to reduce abundance estimation errors in sparse hyperspectral unmixing. It is defined as the difference between the expected abundance computed from the original data and the abundance computed at the superpixel scale using the coarse reconstructed data. This term is constrained by the $\ell_{2,1}$ norm and helps mitigate the influence of mixed noise on the unmixing process.

- 2) A multiscale spectral–spatial regularization method is developed for sparse hyperspectral unmixing. This framework leverages spatial information from multiple levels, including the global image scale, superpixel scale, and 8-neighborhood scale, to improve the accuracy of abundance estimation.

The rest of this article is organized as follows. Section II succinctly elucidates the sparse unmixing model and expatiates the proposed RMSR algorithm. Section III exhibits experimental outcomes utilizing simulated hyperspectral data. Section IV manifests experimental upshots harnessing bona fide hyperspectral datasets. Finally, Section V concludes this article.

II. INNOVATIVE MULTISCALE UNMIXING METHOD

A. Sparse Unmixing Model

Assuming $\mathbf{Y} = [y_1, \dots, y_n] \in \mathbb{R}^{l \times n}$ represents a hyperspectral remote sensing image consisting of n pixels and l spectral bands, $\mathbf{A} = [a_1, \dots, a_m] \in \mathbb{R}^{l \times m}$ is a collection of m endmembers in the spectral library, $\mathbf{X} = [x_1, \dots, x_n] \in \mathbb{R}^{m \times n}$ is the abundance matrix corresponding to each image element in the remote sensing image, and $\mathbf{N} = [n_1, \dots, n_n] \in \mathbb{R}^{l \times n}$ denotes the systematic noise or the potential error. If the spectral library \mathbf{A} is extensive enough to encompass all the endmembers existing in the hyperspectral image [45], then LMM takes the form of

$$\mathbf{Y} = \mathbf{A}\mathbf{X} + \mathbf{N}. \quad (1)$$

LMM is generally subject to two physical constraints, namely, the abundance nonnegativity constraint, represented by $\mathbf{X} \geq 0$, and the abundance sum-to-one constraint (ASC), represented by $\mathbf{1}^T \mathbf{x} = 1$.

Considering that the real number of endmembers in the hyperspectral image is generally fewer than those available in the spectral library, and the abundance matrix \mathbf{X} is generally sparse. Therefore, it is necessary to find the sparse linear combination \mathbf{X} that can optimally represent each of the mixed image elements. The following represents the optimization formulation for sparse unmixing:

$$\min_{\mathbf{X}} \frac{1}{2} \|\mathbf{Y} - \mathbf{A}\mathbf{X}\|_F^2 + \lambda \|\mathbf{X}\|_0 \text{ s.t.: } \mathbf{X} \geq 0 \quad (2)$$

where $\|\mathbf{Y} - \mathbf{A}\mathbf{X}\|_F^2$ denotes the relevant data term, $\|\cdot\|_F$ denotes the Frobenius norm, $\|\mathbf{X}\|_0$ is the indication for the sparsity constraint, and the parameter $\lambda \geq 0$ determines weight given to the regularization term. It should be noted that ASC may not be suitable for sparse unmixing, as the spectral library \mathbf{A} may not contain all the endmember spectra present in \mathbf{Y} [30].

The solution to the ℓ_0 norm is a classical nonconvex optimization problem that is known to be NP-hard [55]. Hence, SUNSAL uses a convex relaxation technique to transform the ℓ_0 constraint into ℓ_1 constraint, as described in the work [56]. The SUNSAL model is denoted as

$$\min_{\mathbf{X}} \frac{1}{2} \|\mathbf{Y} - \mathbf{A}\mathbf{X}\|_F^2 + \lambda \|\mathbf{X}\|_{1,1} \text{ s.t.: } \mathbf{X} \geq 0 \quad (3)$$

where the $\|\mathbf{X}\|_{1,1}$ norm, also known as the $\ell_{1,1}$ norm of \mathbf{X} , is calculated as the sum of the absolute values of each element

within the matrix \mathbf{X} across all its columns. The convex optimization problem is addressed through the alternating directional multiplier method (ADMM) algorithm [57].

B. Superpixel Segmentation

This work adopts the well-known SLIC algorithm [45], [58]. This algorithm clusters pixels locally and iteratively, grouping them together based on their similarity in color (spectrum) and distance. To be more specific, the pixel with the minimum gradient within the neighborhood is selected as the initial clustering seed point to prevent erroneous seed point selection. Thereafter, similar pixels are searched within a region surrounding the seed point for more efficient and focused clustering. Suppose the total number of pixels in the image is N and the desired number of superpixels is K , then the step size of the adjacent seed points in the initial generation is set to $S = \sqrt{\frac{N}{K}}$, and the search range of similar pixels is set to $2S \times 2S$. It enables us to effectively control the granularity of the superpixels according to research needs. Furthermore, we take into account both spatial and spectral information when measuring the similarity between pixels. The spectral angle distance is utilized as a metric to gauge spectral similarity, whereas the Euclidean distance signifies the spatial closeness of the pixels. These similarity measures are defined as follows:

$$d_{\text{spectral}} = \cos^{-1} \left(\frac{\mathbf{x}_p^T \mathbf{x}_q}{\|\mathbf{x}_p\|_2 \|\mathbf{x}_q\|_2} \right) \quad (4)$$

where d_{spectral} is the spectral distance, and \mathbf{x}_p and \mathbf{x}_q are the spectral vectors of pixels p and q in the image, respectively.

$$d_{\text{spatial}} = \sqrt{(p_a - q_a)^2 + (p_b - q_b)^2} \quad (5)$$

where d_{spatial} is the spatial distance, and p_a and p_b denote the spatial position of pixel p .

$$D_{\text{similarity}} = \sqrt{(d_{\text{spectral}})^2 + \left(\frac{d_{\text{spatial}}}{S} \right)^2} w^2 \quad (6)$$

where $D_{\text{similarity}}$ denotes the final similarity metric equation and S is a fixed constant that represents the size of a superpixel block. It is derived from the total pixels and predefined superpixel amount. w is a weight that adjusts the balance between spectral similarity and spatial similarity, with values ranging from 0 to 1. When w is larger, spatial similarity becomes more important, resulting in superpixel blocks with more regular shapes. Conversely, when w is smaller, spectral similarity becomes more important, leading to superpixel blocks with better homogeneity but less regular shapes. Overall, the SLIC algorithm has the advantages of being fast, simple to implement, and capable of generating high-quality superpixel blocks. It can effectively divide a hyperspectral image into multiple coherent and homogeneous regions, forming visually meaningful superpixel blocks.

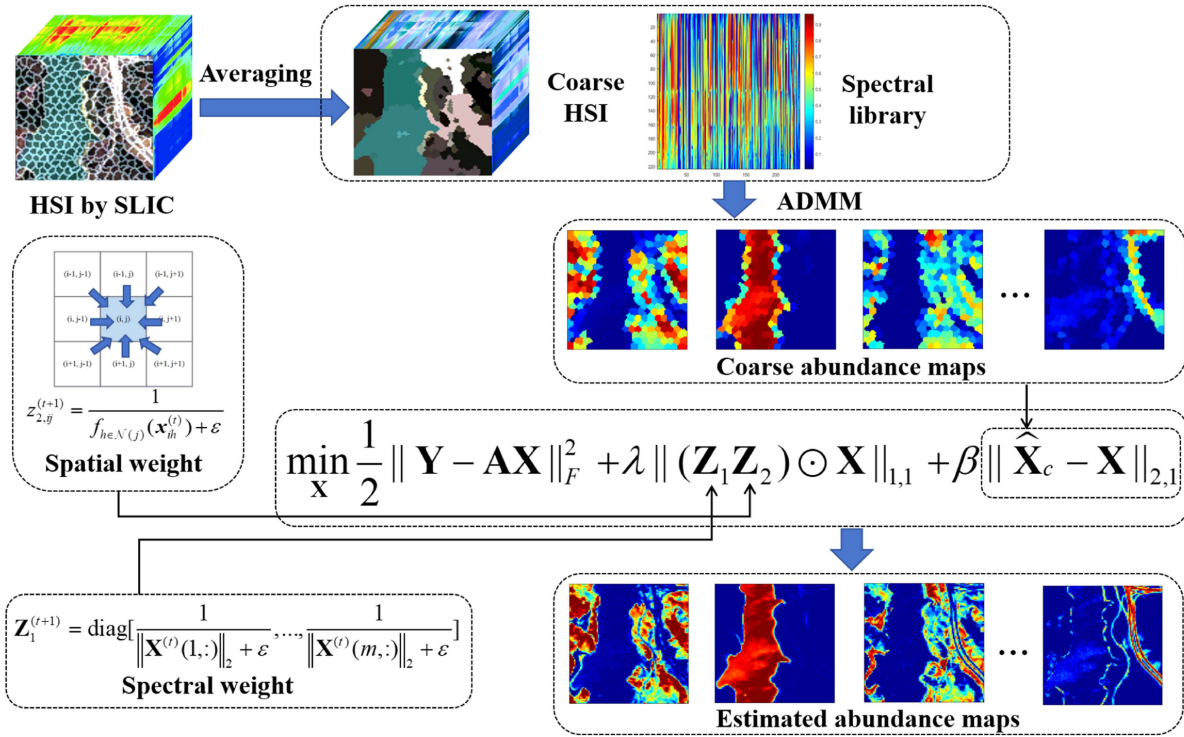


Fig. 1. Flowchart of the proposed RMSR method.

C. Proposed RMSR Model

To enhance the unmixing of hyperspectral images with low signal-to-noise ratio (SNR), effectively utilizing spatial information to mitigate the adverse impact of noise is crucial for improving abundance estimation precision. In addition to leveraging the sparsity of abundances for iterative updates, incorporating reliable spatial and spectral regularization into the unmixing model ensures the stability and accuracy of abundance estimation. Inspired by filter-based image denoising techniques, we proposed a novel multiscale spectral–spatial regularization approach for sparse hyperspectral unmixing, aiming to accurately decompose hyperspectral images severely contaminated by noise.

The workflow diagram of RMSR method is shown in Fig. 1. Initially, the SLIC algorithm introduced in Section II-B is employed to perform superpixel segmentation on the hyperspectral image, followed by averaging the pixels within each superpixel block to generate a new hyperspectral image. This process acts as an approximation of mean filtering, effectively suppressing noise. It is worth mentioning that the proposed RMSR algorithm does not perform preprocessing for denoising. Instead, it primarily reconstructs a rough hyperspectral image using the SLIC algorithm and predictively establishes a superpixel scale abundance matrix. This matrix is then used to construct an $\ell_{2,1}$ regularization term for reducing abundance estimation errors, rather than being directly employed as a solution for abundance estimation. The main purpose of the $\ell_{2,1}$ norm is to induce the abundance of nonzero row vectors to tend toward the desired endmembers. Furthermore, the spectral weight based on the global scale of the image and the spatial weight based on the

8-neighborhood scale are integrated into the $\ell_{1,1}$ norm-based sparse regularization, similar to the work in [51]. Ultimately, the robust multiscale spectral–spatial regularization sparse unmixing (RMSR) model is given by

$$\min_{\mathbf{X}} \frac{1}{2} \|\mathbf{Y} - \mathbf{A}\mathbf{X}\|_F^2 + \lambda \|(\mathbf{Z}_1 \mathbf{Z}_2) \odot \mathbf{X}\|_{1,1} + \beta \|\widehat{\mathbf{X}}_C - \mathbf{X}\|_{2,1} \quad \text{s.t.: } \mathbf{X} \geq 0. \quad (7)$$

The RMSR model consists of three parts. The first term is the data fitting term, the second term is the sparse weighted regularization, and the third term is the superpixel scale spatial regularization. Parameters λ and β adjust the weights of the two regularization terms. Next, the two regularization terms in the model will be explained in detail.

The sparse regularization $\|(\mathbf{Z}_1 \mathbf{Z}_2) \odot \mathbf{X}\|_{1,1}$ introduced two weighting factors into the $\ell_{1,1}$ norm and \odot denotes the multiplication of two variable elements. The spectral weighting factor $\mathbf{Z}_1 \in \mathbb{R}^{m \times m}$ is defined as

$$\mathbf{Z}_1^{(t+1)} = \text{diag} \left[\frac{1}{\|\mathbf{X}^{(t)}(1, :)\|_2 + \varepsilon}, \dots, \frac{1}{\|\mathbf{X}^{(t)}(m, :)\|_2 + \varepsilon} \right] \quad (8)$$

where \mathbf{Z}_1 is a diagonal matrix consists of the ℓ_2 norm of each row vector in \mathbf{X} , $\mathbf{X}^{(t)}$ is the estimated abundance matrix at t iteration, $\|\cdot\|_2$ denotes the ℓ_2 norm, and ε is a small positive constant. The spectral weighting factor will penalize the nonzero rows with smaller values in the whole matrix \mathbf{X} . After multiple iterations, only the rows with significant values are preserved, while the other rows tend to zero. The spatial weighting factor $\mathbf{Z}_2 \in \mathbb{R}^{m \times n}$ is calculated based on the spatial 8-neighborhood

information, and it can be expressed as

$$z_{2,ij}^{(t+1)} = \frac{1}{f_{h \in \mathcal{N}(j)}(\mathbf{x}_{ih}^{(t)}) + \varepsilon} \quad (9)$$

where $z_{2,ij}$ represents an element in the matrix \mathbf{Z}_2 , and the subscripts i and j indicate the row and column indices of the element. The function $f_{h \in \mathcal{N}(j)}(\mathbf{x}_{ih}^{(t)})$ explores the spatial neighborhood information of pixel j . Here, $\mathcal{N}(j)$ denotes the neighboring space surrounding pixel j , and \mathbf{x}_{ih} represents the neighbors of pixel j . The function $f(\cdot)$ is represented as follows:

$$f(\mathbf{x}_{ij}) = \frac{\sum_{h \in \mathcal{N}(j)} \epsilon_{ih} x_{ih}}{\sum_{h \in \mathcal{N}(j)} \epsilon_{ih}} \quad (10)$$

where ϵ_{ih} calculates the Euclidean distance between pixel j and its neighbor \mathbf{x}_{ih} . The spatial weighting factor seeks to leverage spatial context within a local neighborhood. It prioritizes closer pixels by assigning them greater weights, while allotting smaller weights to farther pixels, encouraging center pixel to have similar abundance values with neighboring pixels. When adjacent pixels have low abundances, the abundance of the center pixel will also become smaller iteratively until it is zero. This spatial weighting strategy can simultaneously enhance sparse constraints on the abundances while maintaining spatial coherence of abundance maps.

The superpixel scale spatial regularization $\|\widehat{\mathbf{X}}_C - \mathbf{X}\|_{2,1}$ introduces a precomputed coarse abundance matrix $\widehat{\mathbf{X}}_C$ into the $\ell_{2,1}$ norm as a difference. The coarse abundance matrix $\widehat{\mathbf{X}}_C$ is calculated from a superpixel-based reconstructed hyperspectral image \mathbf{Y}_C . Since \mathbf{Y}_C is reconstructed based on the average of each superpixel in the original hyperspectral image, it acts as a denoiser similar to the mean filter. Therefore, the obtained $\widehat{\mathbf{X}}_C$ is robust to noise. Subsequently, a regularizer based on the $\ell_{2,1}$ norm is introduced to force the sparse unmixing abundance matrix \mathbf{X} to approximate $\widehat{\mathbf{X}}_C$, thereby enhancing the robustness of the algorithm. Let $\mathbf{Y} \in \mathbb{R}^{l \times n}$ be the original hyperspectral image, $\mathbf{Y}_t \in \mathbb{R}^{l \times n_t}$ ($t = 1, \dots, K, \sum_{t=1}^K n_t = n$) represents the t th superpixel obtained by segmenting \mathbf{Y} with the SLIC algorithm. Here, K denotes the number of superpixels and n_t represents the number of pixels in \mathbf{Y}_t . Let $\mathbf{y}_k \in \mathbb{R}^{l \times 1}$ ($k = 1, \dots, n_t$) denote any pixel (column vector) in \mathbf{Y}_t . Based on the aforementioned symbol definitions, the coarse-grained image $\mathbf{Y}_C \in \mathbb{R}^{l \times n}$ can be formulated as

$$\mathbf{y}_c = \frac{1}{n_t} \sum_{k=1}^{n_t} \mathbf{y}_k \quad (11)$$

where \mathbf{y}_c represents any column in the coarse image \mathbf{Y}_C with the same space position in superpixel block \mathbf{Y}_t . It can be seen from (11) that the value of \mathbf{y}_c is the average of all pixel vectors in \mathbf{Y}_t . In other words, the value of each pixel in the coarsened image equates to the average of the aligned superpixel cluster in the native image. The source image is projected onto the reconstituted coarse image at a superpixel-by-superpixel.

Subsequently, the coarse abundance matrix $\widehat{\mathbf{X}}_C$ is obtained through a coarse decomposition of the coarse image \mathbf{Y}_C . In this process, SUnSAL algorithm is employed for the solution, as

follows:

$$\begin{aligned} \widehat{\mathbf{X}}_C = \arg \min_{\mathbf{X}_C} & \frac{1}{2} \|\mathbf{Y}_C - \mathbf{A}\mathbf{X}_C\|_F^2 \\ & + \lambda_c \|\mathbf{X}_C\|_{1,1} \quad \text{s.t.: } \mathbf{X}_C \geq 0. \end{aligned} \quad (12)$$

The coarse abundance matrix $\widehat{\mathbf{X}}_C$ preserves the correlation among each pixel and its neighboring pixels within the same superpixel. It can be incorporated into the unmixing model in multiple ways. To enforce concordance between the coarse abundance and predicted abundance, constraints can be imposed on their divergence. The Frobenius norm, $\ell_{1,1}$ norm, and $\ell_{2,1}$ norm can be utilized for constraining these differences. However, it should be noted that the Frobenius norm is indeed defined as the square root of the sum of the squares of a matrix's elements, which measures the magnitude of a matrix. When the matrix is defined as the difference between the coarse abundance and predicted abundance, the Frobenius norm constraint is excessively stringent, leading to an excessive reliance on the coarse abundance. Alternatively, the $\ell_{1,1}$ norm is computed as the sum of the absolute values of the matrix elements. It only takes into account individual pixels and ignores potential collaborative relationships among them. The $\ell_{2,1}$ norm calculates the sum of the squared magnitudes of the rows of a matrix, followed by taking the square root of the resulting sum. The minimization of $\ell_{2,1}$ norm captures the combined contribution of multiple rows while penalizing minor values in an effort to encourage row sparsity. The $\ell_{2,1}$ norm constraint further facilitates the consistency of endmembers in the coarse abundance and inferred abundance. Consequently, we introduce the coarse abundance matrix as differences within the framework of the $\ell_{2,1}$ norm.

The proposed RMSR model leverages the spatial and spectral information of hyperspectral images at multiple scales, including the global scale, 8-neighborhood scale, and superpixel scale. It incorporates two regularization terms: a spatial–spectral weighted $\ell_{1,1}$ norm and an $\ell_{2,1}$ norm of the divergence between the superpixel-based coarse-grained abundance and the predicted abundances. The spatial–spectral weighted $\ell_{1,1}$ norm encourages both spatial coherence and spectral sparsity in the estimated abundance maps, promoting the identification of distinct materials and reducing the influence of noise. The $\ell_{2,1}$ norm reduces discrepancies between the coarse-grained and inferred abundance, preserving the spatial structure within each superpixel and enhancing the coherence of the estimated abundances in a homogeneous region. By incorporating multiscale constraints, the RMSR model improves the accuracy and reliability of abundance estimation in hyperspectral image analysis.

D. Optimal Solution Approach

This section demonstrates the application of ADMM to solve the proposed RMSR model. It provides a detailed explanation of solving (7). To facilitate the solution, first of all, (7) is modified to the following form:

$$\min_{\mathbf{X}} \frac{1}{2} \|\mathbf{Y} - \mathbf{A}\mathbf{X}\|_F^2 + \lambda \|(\mathbf{Z}_1 \mathbf{Z}_2) \odot \mathbf{X}\|_{1,1}$$

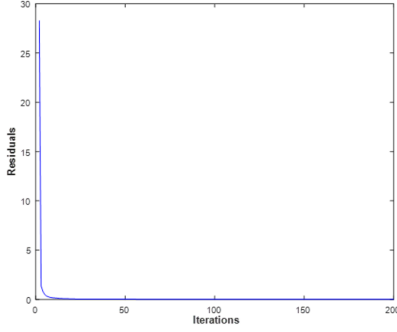


Fig. 2. Residual $\|\mathbf{G}\mathbf{U}^{(t)} + \mathbf{B}\mathbf{V}^{(t)}\|_F$ versus outer loop iterations for the proposed algorithm.

$$+ \beta \|\widehat{\mathbf{X}}_C - \mathbf{X}\|_{2,1} + l_{\mathbb{R}^+}(\mathbf{X}) \quad (13)$$

where $l_{\mathbb{R}^+}(\mathbf{X}) = \sum_{i=1}^n l_{\mathbb{R}^+}(\mathbf{x}_i)$ is an indicator function. It equals zero if \mathbf{x}_i is nonnegative, and positive infinity otherwise.

To alleviate the intricacy of solving the original objective function, five auxiliary variables \mathbf{U} , \mathbf{V}_1 , \mathbf{V}_2 , \mathbf{V}_3 , and \mathbf{V}_4 are introduced as

$$\begin{aligned} \min_{\mathbf{U}, \mathbf{V}_1, \mathbf{V}_2, \mathbf{V}_3, \mathbf{V}_4} & \frac{1}{2} \|\mathbf{Y} - \mathbf{V}_1\|_F^2 + \lambda \|(\mathbf{Z}_1 \mathbf{Z}_2) \odot \mathbf{V}_2\|_{1,1} \\ & + \beta \|\widehat{\mathbf{X}}_C - \mathbf{V}_3\|_{2,1} + l_{\mathbb{R}^+}(\mathbf{V}_4) \\ \text{s.t.} & \mathbf{V}_1 = \mathbf{A}\mathbf{U}, \mathbf{V}_2 = \mathbf{U}, \mathbf{V}_3 = \mathbf{U}, \mathbf{V}_4 = \mathbf{U}. \end{aligned} \quad (14)$$

We rewrite (14) in a compact form

$$\min_{\mathbf{U}, \mathbf{V}} g(\mathbf{U}, \mathbf{V}) \quad \text{s.t.} \quad \mathbf{G}\mathbf{U} + \mathbf{B}\mathbf{V} = \mathbf{0} \quad (15)$$

where $g(\mathbf{U}, \mathbf{V}) = \frac{1}{2} \|\mathbf{Y} - \mathbf{V}_1\|_F^2 + \lambda \|(\mathbf{Z}_1 \mathbf{Z}_2) \odot \mathbf{V}_2\|_{1,1} + \beta \|\widehat{\mathbf{X}}_C - \mathbf{V}_3\|_{2,1} + l_{\mathbb{R}^+}(\mathbf{V}_4)$, $\mathbf{G} = (\mathbf{A}, \mathbf{I}, \mathbf{I}, \mathbf{I})^T$, and $\mathbf{B} = \text{diag}(-\mathbf{I})$, $\mathbf{V} = (\mathbf{V}_1, \mathbf{V}_2, \mathbf{V}_3, \mathbf{V}_4)^T$. Followed by the introduction of the Lagrange multiplier $\mathbf{D} = (\mathbf{D}_1, \mathbf{D}_2, \mathbf{D}_3, \mathbf{D}_4)^T$, the augmented Lagrangian of (14) can be expressed as follows:

$$\mathcal{L}(\mathbf{U}, \mathbf{V}, \mathbf{D}) = g(\mathbf{U}, \mathbf{V}) + \frac{\mu}{2} \|\mathbf{G}\mathbf{U} + \mathbf{B}\mathbf{V} - \mathbf{D}\|_F^2 \quad (16)$$

where μ is a positive constant. Subsequently, we leverage the ADMM to solve the associated optimization problem, as delineated in Algorithm 1. $\text{soft}(y, \tau) = \text{sign}(y) \max\{|y| - \tau, 0\}$ is the soft-threshold function, $\text{vect} - \text{soft}(y, \tau) = y \frac{\max\{|y| - \tau, 0\}}{\max\{|y| - \tau, \tau\}}$ is the vect-soft threshold function, and u and d_2 are the entries in \mathbf{U} and \mathbf{D}_2 , respectively.

The plot in Fig. 2 shows the image of the residual plotted versus the iteration count. The number of iterations is set based on experience to 5 and 200 for the interior and exterior cycles, respectively. The minimum threshold for the residual $\|\mathbf{G}\mathbf{U}^{(t)} + \mathbf{B}\mathbf{V}^{(t)}\|_F$ is set to 10^{-5} . It can be observed that Algorithm 1 converges quickly and is nearby converging to zero after 50 iterations.

III. SIMULATION DATA EXPERIMENTS AND ANALYSIS

In this section, to ascertain the efficacy of the proposed RMSR approach, it is compared with the results obtained from

Algorithm 1: ADMM Method for Solving (7).

- 1: **Input:**
- 2: \mathbf{Y} , \mathbf{A} , \mathbf{X}_C , parameters $\lambda, \beta, \mathcal{E}, k = 0, t = 0, \mu > 0$ and initialize $\mathbf{U}^{(0)} = \mathbf{0}, \mathbf{V}_1^{(0)} = \mathbf{V}_2^{(0)} = \mathbf{V}_3^{(0)} = \mathbf{V}_4^{(0)} = \mathbf{0}$.
- 3: **Repeat:**
- 4: $\mathbf{Z}_1^{(t)} \leftarrow \text{diag} \left[\frac{1}{\|(\mathbf{U}^{(t)} - \mathbf{D}_2^{(t)})(1,:)\|_2 + \mathcal{E}}, \dots, \frac{1}{\|(\mathbf{U}^{(t)} - \mathbf{D}_2^{(t)})(m,:)\|_2 + \mathcal{E}} \right]$
- 5: $\mathbf{Z}_2^{(t)} \leftarrow \begin{bmatrix} z_{2,11}^{(t)} & \cdots & z_{2,1n}^{(t)} \\ \vdots & z_{2,ij}^{(t)} & \vdots \\ z_{2,m1}^{(t)} & \cdots & z_{2,mn}^{(t)} \end{bmatrix}$
- 6: where $z_{2,ij}^{(t)} = \frac{1}{f_{h \in \mathcal{N}(j)}(u_{ih}^{(t)} - d_{2,ih}^{(t)}) + \mathcal{E}}$
- 7: **Repeat:**
- 8: $\mathbf{U}^{(k+1)} \leftarrow (\mathbf{A}^T \mathbf{A} + 3\mathbf{I})^{-1} (\mathbf{A}^T (\mathbf{V}_1^{(k)} + \mathbf{D}_1^{(k)}) + \mathbf{V}_2^{(k)} + \mathbf{D}_2^{(k)} + \mathbf{V}_3^{(k)} + \mathbf{D}_3^{(k)} + \mathbf{V}_4^{(k)} + \mathbf{D}_4^{(k)})$
- 9: $\mathbf{V}_1^{(k+1)} = \frac{1}{1+\mu} [\mathbf{Y} + \mu (\mathbf{A}\mathbf{U}^{(k+1)} - \mathbf{D}_1^{(k)})]$
- 10: $\mathbf{V}_2^{(k+1)} = \text{soft}(\mathbf{U}^{(k+1)} - \mathbf{D}_2^{(k)}, \frac{\lambda}{\mu} \mathbf{Z}_1^{(t)} \mathbf{Z}_2^{(t)})$
- 11: $\mathbf{V}_3^{(k+1)} = \text{vect} - \text{soft}(\mathbf{U}^{(k+1)} - \mathbf{D}_3^{(k)} - \widehat{\mathbf{X}}_C, \frac{\beta}{\mu}) + \widehat{\mathbf{X}}_C$
- 12: $\mathbf{V}_4^{(k+1)} = \max(\mathbf{U}^{(k+1)} - \mathbf{D}_4^{(k)}, 0)$
- 13: **Update Lagrange multipliers:**
- 14: $\mathbf{D}_1^{(k+1)} \leftarrow \mathbf{D}_1^{(k)} - \mathbf{A}\mathbf{U}^{(k+1)} + \mathbf{V}_1^{(k+1)}$
- 15: $\mathbf{D}_2^{(k+1)} \leftarrow \mathbf{D}_2^{(k)} - \mathbf{U}^{(k+1)} + \mathbf{V}_2^{(k+1)}$
- 16: $\mathbf{D}_3^{(k+1)} \leftarrow \mathbf{D}_3^{(k)} - \mathbf{U}^{(k+1)} + \mathbf{V}_3^{(k+1)}$
- 17: $\mathbf{D}_4^{(k+1)} \leftarrow \mathbf{D}_4^{(k)} - \mathbf{U}^{(k+1)} + \mathbf{V}_4^{(k+1)}$
- 18: **Update iteration:** $k \leftarrow k + 1$
- 19: $\mathbf{U}^{(t+1)} \leftarrow \mathbf{U}^{(k+1)}$
- 20: $\mathbf{D}_2^{(t+1)} \leftarrow \mathbf{D}_2^{(k+1)}$
- 21: **Update iteration:** $t \leftarrow t + 1$
- 22: **until** the termination condition is met.

five advanced sparse unmixing algorithms: ADSpLRU [59], JSpBLRU [60], DRSU-TV [44], MUA (SLIC) [50], and S²WSU [51]. Three evaluation metrics, including signal-to-reconstruction error (SRE, measured in dB), the probability of success (p_s), and *sparsity*, were harnessed to calibrate the functionality of each unmixing method. The definition of SRE (dB) is delineated henceforth

$$\text{SRE (dB)} = 10 \log_{10} \left(\frac{E(\|\mathbf{x}\|_2^2)}{E(\|\mathbf{x} - \widehat{\mathbf{x}}\|_2^2)} \right). \quad (17)$$

In the preceding equation, \mathbf{x} and $\widehat{\mathbf{x}}$ symbolize the veritable fractional abundances and surmised abundances severally, while $E(\cdot)$ emblemizes the expectation operator.

The probability of success (p_s) mentioned in [30] proffers an intimation regarding the robustness of the appraisal. It is defined as follows:

$$p_s \equiv P(\|\widehat{\mathbf{x}} - \mathbf{x}\|^2 / \|\mathbf{x}\|^2 \leq \text{threshold}). \quad (18)$$

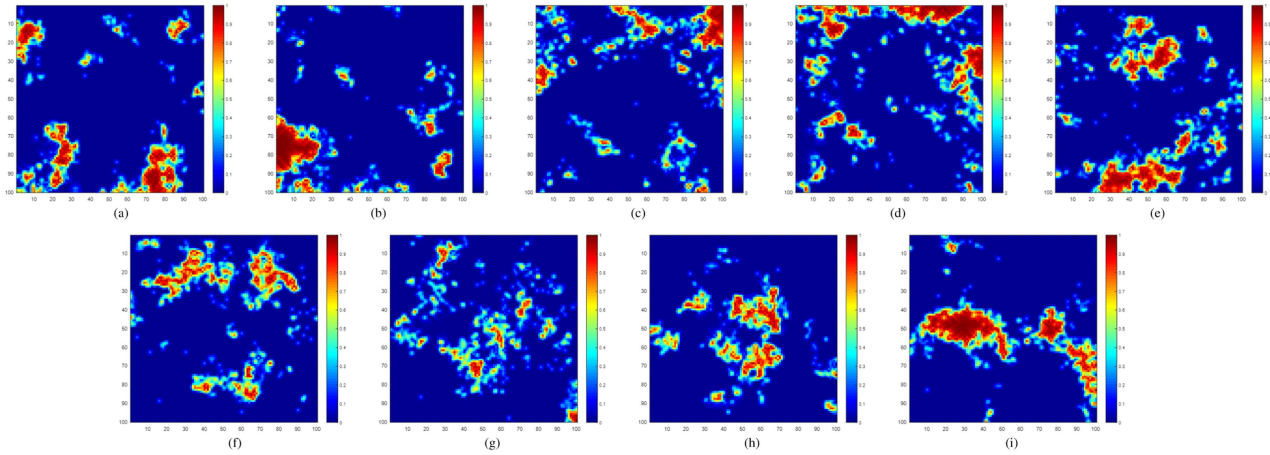


Fig. 3. Ground truth fractional abundance maps of the endmembers in SDC1. (a)–(i) Endmember #1–#9.

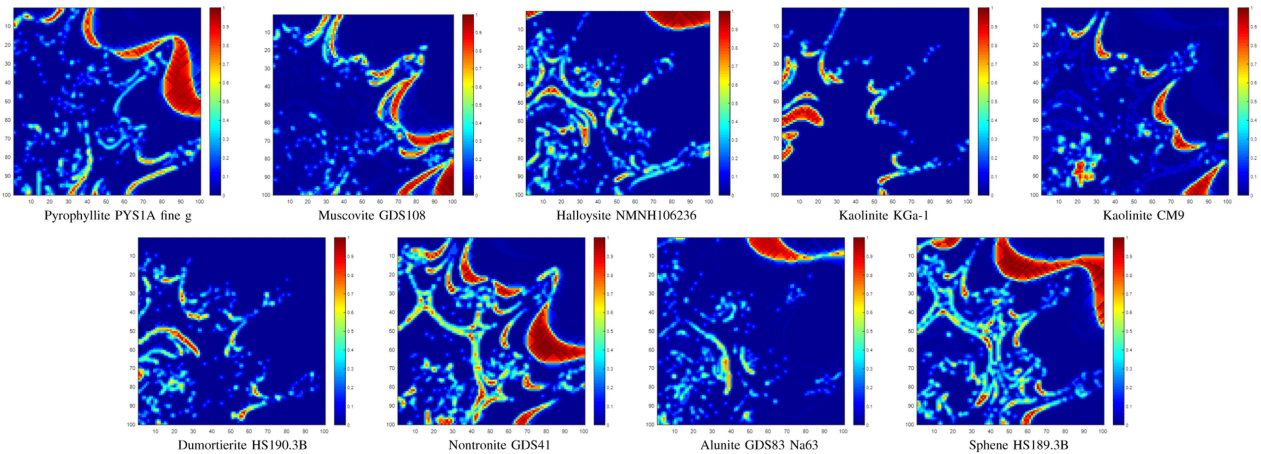


Fig. 4. Ground truth abundance maps of SDC2.

The optimal performance threshold is defined as 3.16 (5 dB) according to [30]. Elevated SRE (dB) or p_s magnitudes portend superior unmixing functionality. Specifically, *sparsity* is defined as the fraction of nonzero entries (elements with coefficient values greater than 0.005) in $\hat{\mathbf{x}}$ relative to the total number of entries. It is evident that as the sparsity decreases, the unmixing solution becomes sparser.

A. Simulated Datasets

The simulated data experiment employs two mineral spectral libraries, both being subsets of the USGS library.¹ The premier spectral library $\mathbf{A}_1 \in \mathbb{R}^{224 \times 240}$ subsumes 240 materials with 224 bands spaced at regular intervals throughout the 0.4–2.5 μm electromagnetic wavelength territory. The latter spectral library $\mathbf{A}_2 \in \mathbb{R}^{221 \times 222}$ encompasses 222 materials with 221 bands equipartitioned over the 0.4–2.5 μm electromagnetic wavelength domain. Adhering to the precepts of the linear spectral mixing model, we fabricated two simulated datasets from the aforementioned spectral libraries.

- 1) *Simulated Data Cube 1 (SDC1)*: A data cube named SDC1 was created, containing 100×100 pixels with 224 spectral bands per pixel. The generation process involved randomly selecting nine spectral signatures from \mathbf{A}_1 , as documented in [43]. The fractional abundances exhibit a piecewise smoothness property, which helps in revealing the spatial information mining capabilities of different algorithms. A pictographic representation of the authentic endmember abundance distribution is given in Fig. 3.
- 2) *Simulated Data Cube 2 (SDC2)*: SDC2 encompasses 100×100 pixels, and each endowed with 221 bands. As portrayed in [61], nine particular endmembers were selected from \mathbf{A}_2 . The abundance maps deftly simulate the spatial dissemination of archetypal landforms existent in the world around us. Fig. 4 provides imagery of the percent abundance layouts corresponding to each individual endmember.

¹[Online] Available: <http://speclab.cr.usgs.gov/spectral.lib06>

TABLE I
RESULTS OF SRE (dB), p_s , AND SPARSITY FOR VARIOUS ALGORITHMS ON SDC1

Algorithm	SNR=20dB			SNR=30dB			SNR=40dB		
	SRE (dB)	p_s	sparsity	SRE (dB)	p_s	sparsity	SRE (dB)	p_s	sparsity
ADSpLRU	6.5590	0.7387	0.0501	18.6708	0.9966	0.0157	29.2021	1	0.0122
	$(\lambda = 18, \tau = 7e-3)$			$(\lambda = 2, \tau = 1e-3)$			$(\lambda = 8e-1, \tau = 2e-4)$		
JSpBLRU	4.5873	0.6156	0.0754	12.2822	0.9395	0.0244	28.2473	1	0.0155
	$(\lambda = 13, \tau = 17)$			$(\lambda = 2, \tau = 4)$			$(\lambda = 1, \tau = 2e-1)$		
DRSU-TV	8.4184	0.8438	0.0379	19.3229	0.9937	0.0260	31.1984	1	0.0127
	$(\lambda = 8e-3, \lambda_{TV} = 2e-2)$			$(\lambda = 3e-3, \lambda_{TV} = 2e-3)$			$(\lambda = 2e-3, \lambda_{TV} = 4e-4)$		
MUA	7.4257	0.7372	0.0655	11.0458	0.9259	0.0561	16.0422	0.9973	0.0415
	$(\lambda = 1e-1, \beta = 2)$			$(\lambda = 2e-2, \beta = 2e-1)$			$(\lambda = 6e-3, \beta = 2e-2)$		
S ² WSU	8.0178	0.8146	0.0296	21.7501	0.9994	0.0152	32.2263	1	0.0123
	$(\lambda = 9e-3)$			$(\lambda = 5e-3)$			$(\lambda = 2e-3)$		
RMSR	14.1040	0.9794	0.0159	23.0452	0.9999	0.0133	32.3335	1	0.0123
	$(\lambda = 3e-2, \beta = 6e-1)$			$(\lambda = 8e-3, \beta = 1e-1)$			$(\lambda = 2e-3, \beta = 2e-2)$		
RMSR _F	12.8257	0.9584	0.0162	22.9624	0.9996	0.0133	32.2593	1	0.0123
	$(\lambda = 3e-2, \beta = 5e-2)$			$(\lambda = 9e-3, \beta = 8e-3)$			$(\lambda = 2e-3, \beta = 2e-3)$		

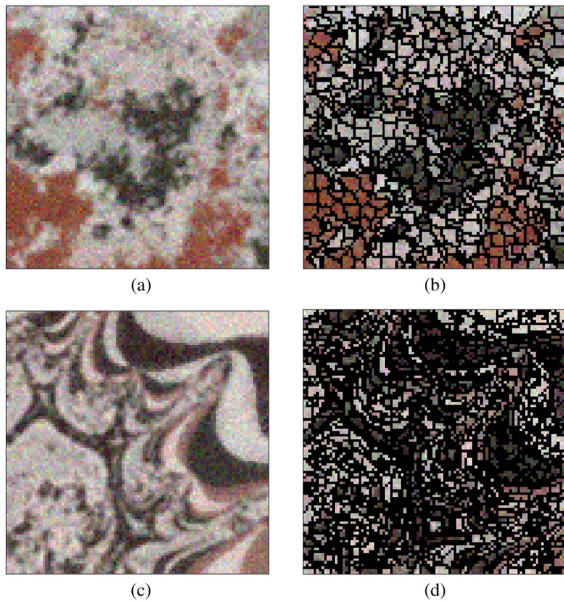


Fig. 5. Segmentation results on the simulated data at the SNR of 20 dB by the SLIC method. (a) Pseudocolor image of SDC1. (b) Segmentation result. (c) Pseudocolor image of SDC2. (d) Segmentation result.

Thereafter, independent and identically distributed Gaussian noise was introduced to the two simulated datasets, resulting in datasets with SNR of 20, 30, and 40 dB, respectively.

B. Results and Discussion

Fig. 5(a) and (c) shows the false-color images of randomly selected bands from two simulated datasets with an SNR of 20 dB, respectively. Fig. 5(b) and (d) demonstrates the segmentation results of the two simulated datasets using the SLIC algorithm, respectively. As can be seen from the figures,

the SLIC segmentation technique can effectively extract the homogeneity information of images and still achieve relatively good segmentation performance on datasets with low SNRs. This advances the effectiveness of unmixing methods. In light of the aforementioned, both the RMSR algorithm and the MUA algorithm devised herein leverage the SLIC technique to partition the imagery.

Tables I and II, respectively, present the SRE (dB), p_s values, and sparsity attained by diverse sparse unmixing algorithms operating on SDC1 and SDC2 across all three SNR tiers. The optimal parametric configurations availing the utmost performance from each algorithm are denoted within parentheses. To further validate the performance of the regularization term for reducing the abundance estimation error introduced in the RMSR unmixing model, we impose constraints on it through Frobenius norm (defined as RMSR_F) and $\ell_{2,1}$ norm (i.e., RMSR), respectively. Examination of Tables I and II illuminate that the RMSR algorithm propounded herein attains superior SRE (dB) and p_s metrics compared with alternative unmixing methods across most scenarios under consideration. The RMSR_F algorithm achieved suboptimal values comparable to the RMSR algorithm in most cases. Especially at low SNR, the superiority of the two algorithms is more prominent. This indicates that our method has good noise robustness. Relative to the MUA algorithm, the RMSR algorithm propounded herein incorporates spectral weighting predicated on holistic image scale and spatial weighting derived from local eight-pixel vicinities, conferring considerable enhancements in unmixing capabilities. Relative to the S²WSU algorithm, the RMSR algorithm propounded herein incorporates a regularization component designed to diminish deviations in abundance estimates, thereby mitigating pernicious impacts of noise upon unmixing performance. To further validate the performance of the regularization term for reducing the abundance estimation error introduced in the RMSR unmixing model, we impose constraints on it through Frobenius

TABLE II
RESULTS OF SRE (dB), p_s , AND SPARSITY FOR VARIOUS ALGORITHMS ON SDC2

Algorithm	SNR=20dB			SNR=30dB			SNR=40dB		
	SRE (dB)	p_s	sparsity	SRE (dB)	p_s	sparsity	SRE (dB)	p_s	sparsity
ADSpLRU	6.4044	0.6807	0.0701	16.4287	0.9828	0.0306	25.0912	1	0.0189
	$(\lambda = 18, \tau = 4e-3)$			$(\lambda = 2, \tau = 4e-4)$			$(\lambda = 1, \tau = 7e-5)$		
JSpBLRU	3.8108	0.5078	0.0790	15.1094	0.9926	0.0489	24.9620	1	0.0236
	$(\lambda = 24, \tau = 43)$			$(\lambda = 2, \tau = 9e-1)$			$(\lambda = 7e-1, \tau = 1e-1)$		
DRSU-TV	9.3255	0.8222	0.0543	19.3229	0.9937	0.0260	27.6420	1	0.0221
	$(\lambda = 2e-3, \lambda_{TV} = 2e-2)$			$(\lambda = 3e-3, \lambda_{TV} = 2e-3)$			$(\lambda = 6e-4, \lambda_{TV} = 4e-4)$		
MUA	5.3248	0.5026	0.0837	8.0303	0.7205	0.0813	12.6404	0.9388	0.0661
	$(\lambda = 1e-1, \beta = 3)$			$(\lambda = 7e-3, \beta = 3e-1)$			$(\lambda = 2e-3, \beta = 3e-2)$		
S ² WSU	5.6842	0.6836	0.0238	19.7573	0.9926	0.0207	27.8067	1	0.0215
	$(\lambda = 1e-2)$			$(\lambda = 3e-3)$			$(\lambda = 4e-4)$		
RMSR	13.2162	0.9387	0.0201	20.4129	0.9981	0.0202	28.1130	1	0.0210
	$(\lambda = 3e-2, \beta = 7e-1)$			$(\lambda = 4e-3, \beta = 2e-1)$			$(\lambda = 5e-4, \beta = 2e-2)$		
RMSR _F	12.7928	0.9266	0.0194	20.0245	0.9965	0.0206	28.0653	0.9999	0.0209
	$(\lambda = 4e-2, \beta = 4e-2)$			$(\lambda = 3e-3, \beta = 8e-3)$			$(\lambda = 5e-4, \beta = 9e-4)$		

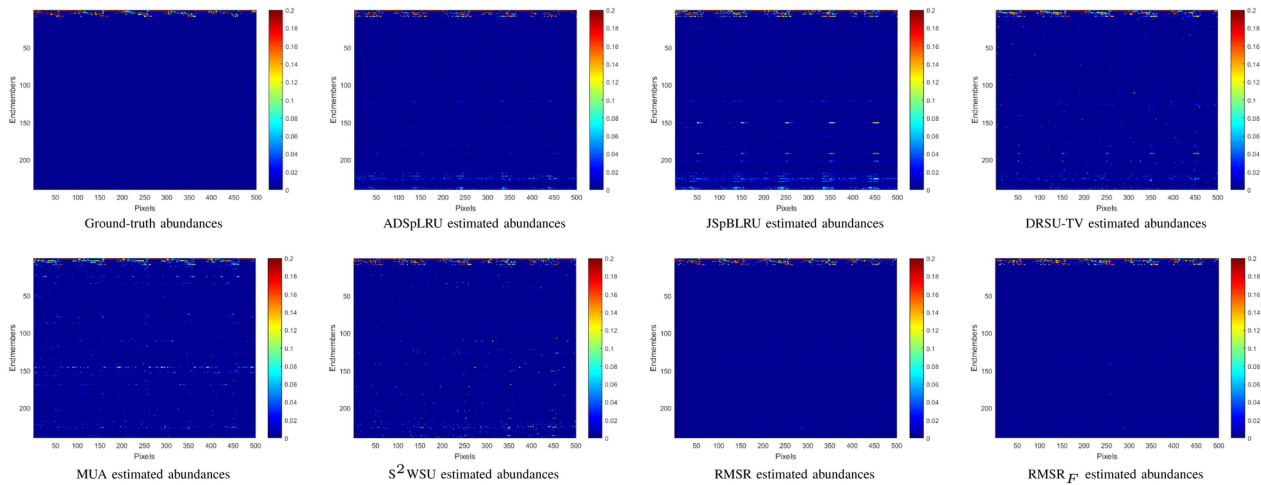


Fig. 6. Abundance maps garnered through various methods on SDC1 data under SNR = 20 dB (solely 500 pixels exhibited).

norm (defined as RMSR_F) and $\ell_{2,1}$ norm, respectively. The empirical findings indicate that utilizing the $\ell_{2,1}$ norm yielded superior SRE (dB) and p_s values outcomes, especially under low SNR conditions, which further validates the effectiveness of this relaxation method.

To facilitate a more intuitive comparison, Figs. 6 and 7 showcase the real abundances and inferred fractional abundances achieved by varied algorithms on SDC1 and SDC2 individually, with an SNR of 20 dB. For perspicuity, merely 500 stochastically chosen pixels from the outcomes are rendered, with chromatic traces denoting the proportions of the endmembers. By analyzing Figs. 6 and 7, we can discern that the inferred abundance diagrams produced by our postulated RMSR technique exhibit superior visual quality, showcasing negligible erroneous demarcations. The chromatic demarcations in these illustrations intimately emulate the delineations in the authentic abundance

maps, both regarding their multitude and spatial juxtaposition. The figures clearly illustrate that the results obtained by the MUA algorithm are heavily impacted by noise interference, rendering them excessively noisy. The abundance maps educed by the duo of methods ADSpLRU and JSpBLRU, both of which impose low-rank constraints, are imbued with a proliferation of spurious delineations. There exist conspicuous divergences between the fractional abundance representations fabricated by the S²WSU and DRSU-TV approaches and the factual fractional abundance portrayals. To summarize, it corroborates that our proposed approach possesses superior noise-immunity capabilities.

In order to provide a more comprehensive evaluation of the performance of our proposed RMSR algorithm, Fig. 8 depicts the inferred abundance representations of the ninth endmember in SDC1 under an SNR of 20 dB (similar observations can be made for other endmembers). In addition, the illustration

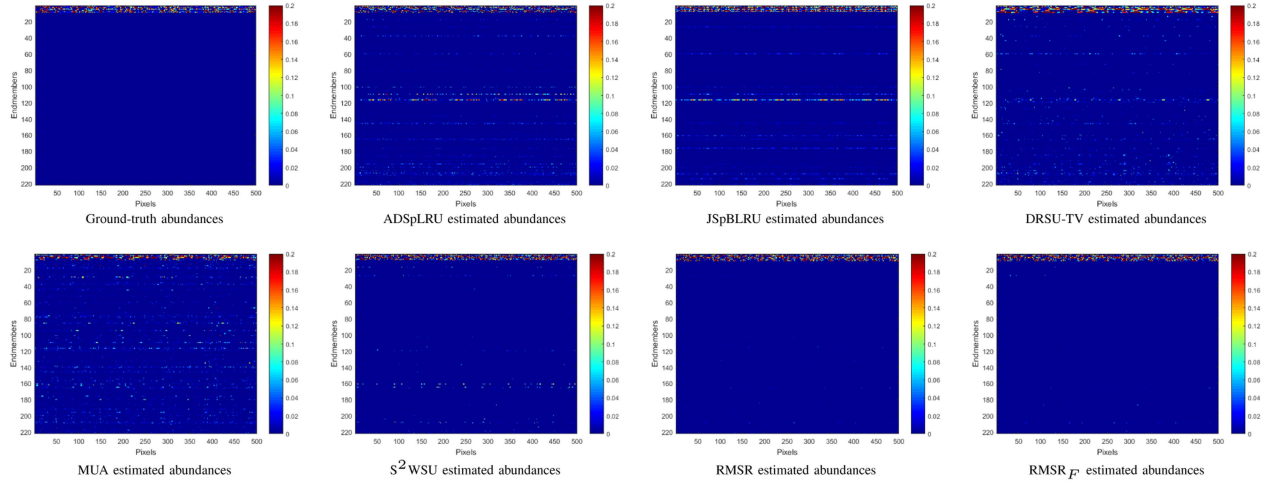


Fig. 7. Abundance maps garnered through various methods on SDC2 data under SNR=20 dB (solely 500 pixels exhibited).

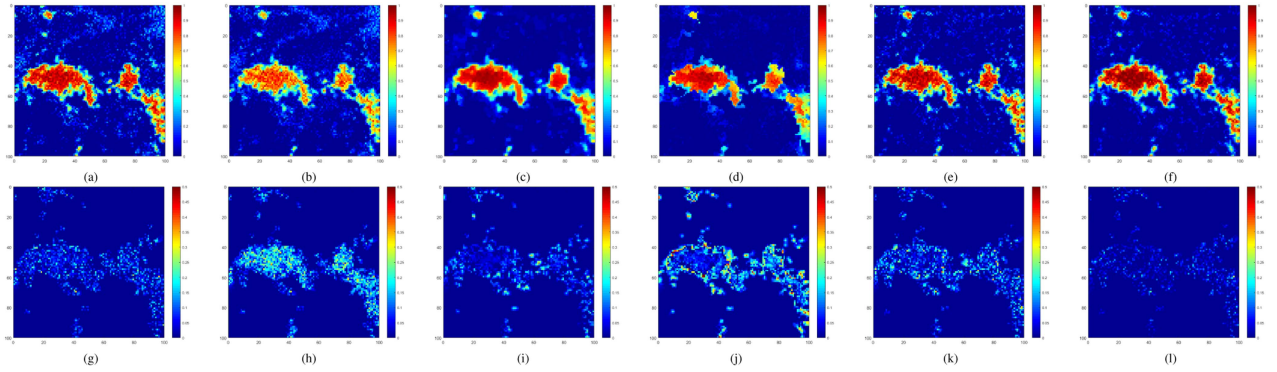


Fig. 8. (a)–(f) Abundance maps of the ninth endmember garnered via unmixing the SCD1 data at an SNR of 20 dB using various algorithms. (g)–(l) Deviation maps between the factual abundance maps and the inferred ones by each algorithm. (a) ADSpLRU. (b) JSpBLRU. (c) DRSU-TV. (d) MUA. (e) S^2WSU . (f) RMSR. (g) ADSpLRU. (h) JSpBLRU. (i) DRSU-TV. (j) MUA. (k) S^2WSU . (l) RMSR.

exhibits deviation portrayals between the inferred abundance and the factual abundance evaluated by diverse unmixing methods. It is evident that the RMSR algorithm produces results that are less affected by noise, accurately representing each abundance fraction region. Particularly in areas with high-abundance fractions, the RMSR algorithm preserves more detailed texture information and exhibits minimal deviation from the true abundance values. The abundance maps obtained through the ADSpLRU and JSpBLRU algorithms exhibit a significant amount of noise. On the other hand, the MUA algorithm lacks adequate utilization of spatial information within the image, leading to lower estimation accuracy. The DRSU-TV algorithm, which incorporates TV regularization, tends to oversmooth the estimated abundance maps, resulting in a loss of fine image details, particularly in edge areas. On the other hand, the S^2WSU algorithm only considers the abundance estimation of neighboring pixels within local windows, resulting in the presence of some noisy points in the inferred abundance maps.

Fig. 9 provides a visual appraisal of the inferred abundance portrayals of the seventh endmember on the SDC2 dataset (SNR = 20 dB) obtained from various unmixing algorithms,

alongside the associated divergence representations between the approximated and factual abundances. These outcomes enable us to evaluate the precision capability of each algorithm. Analogous deductions can be gleaned as in Fig. 8. The unmixing performance of MUA algorithm is poor. The estimated abundance image by DRSU-TV algorithm is still oversmoothed. S^2WSU and JSpBLRU algorithms are more susceptible to noise interference. In comparison, the proposed RMSR algorithm suffers the least from noise interference on the SDC2 dataset, demonstrating good noise-resistance capabilities. Upon examining the difference map of the simulated SDC2 data, it is apparent that the abundance map estimated by our algorithm exhibits the least deviation from the true abundance values. This observation aligns with the findings obtained from the comparative experiment discussed earlier in the previous section. In summary, by exploiting the spatial information in the image from multiple perspectives, the proffered RMSR method accomplishes the overall optimum competence.

To further demonstrate the performance of the proposed algorithm in handling sparse noise in images, we introduced two types of sparse noise, namely impulse noise and dead lines, on

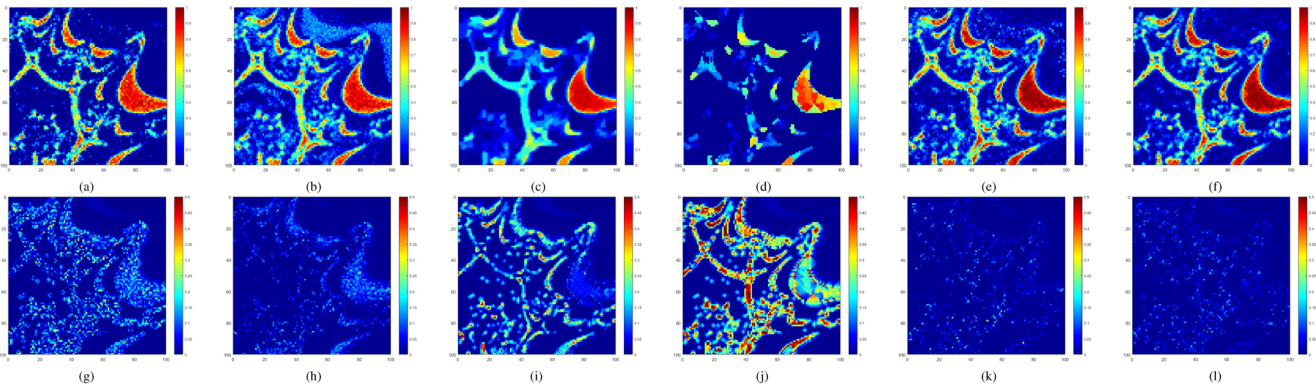


Fig. 9. (a)–(f) Abundance maps of the seventh endmember garnered via unmixing the SDC2 data at an SNR of 20 dB using various algorithms. (g)–(l) Deviation maps between the factual abundance maps and the inferred ones by each algorithm. (a) ADSpLRU. (b) JSpBLRU. (c) DRSU-TV. (d) MUA. (e) S^2 WSU. (f) RMSR. (g) ADSpLRU. (h) JSpBLRU. (i) DRSU-TV. (j) MUA. (k) S^2 WSU. (l) RMSR.

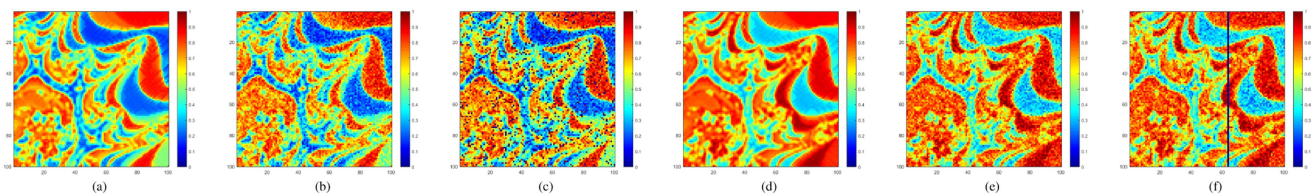


Fig. 10. (a) Band 20 of SDC2 without any noise interference. (b) Gaussian noise with an SNR of 20 dB added on top of (a). (c) Impulse noise added on top of (b). (d) Band 80 of SDC2 without any noise interference. (e) Gaussian noise with an SNR of 20 dB added on top of (d). (f) Dead lines added on top of (e).

TABLE III
RESULTS OF SRE(dB) AND p_s FOR VARIOUS ALGORITHMS ON THE SDC2 CORRUPTED BY SPARSE NOISE

Algorithm	ADSpLRU		JSpBLRU		DRSU-TV		MUA		S^2 WSU		RMSR	
	SRE (dB)	p_s	SRE (dB)	p_s	SRE (dB)	p_s	SRE (dB)	p_s	SRE (dB)	p_s	SRE (dB)	p_s
SNR=20dB	3.8375	0.5057	1.5803	0.2257	4.9386	0.5724	3.9660	0.3853	4.6714	0.5829	10.3776	0.8560
	$(\lambda = 26, \tau = 9e-3)$		$(\lambda = 11, \tau = 31)$		$(\lambda = 1e-2, \lambda_{TV} = 2e-2)$		$(\lambda = 3e-1, \beta = 5)$		$(\lambda = 7e-2)$		$(\lambda = 4e-2, \beta = 8e-1)$	

TABLE IV
RUNTIMES (IN SECONDS) OF VARIOUS UNMIXING METHODS ON PROCESSING SDC2 AT SNR = 20 dB

Algorithm	ADSpLRU	JSpBLRU	DRSU-TV	MUA	S^2 WSU	RMSR
Times(s)	264.91	234.74	451.83	8.19	74.10	131.14

top of the SDC2 dataset with an SNR of 20 dB. Specifically, bands 20–30 and 150–160 were contaminated with 10% impulse noise, whereas bands 80–90 and 180–190 were contaminated with dead lines. For this hyperspectral image corrupted by multiple types of noise, we selected images from bands 20 and 80 for visualization, as shown in Fig. 10.

Table III presents the SRE (dB) and p_s values achieved by various unmixing algorithms under sparse noise interference. The optimal parameter configurations for each algorithm are also indicated within parentheses. It can be observed from Table III that the proposed RMSR algorithm exhibits superior performance in terms of SRE (dB) and p_s values compared with other unmixing methods. The SRE (dB) value reaches an impressive 10 dB, while none of the other algorithms surpass 5 dB.

This indicates that the proposed RMSR method demonstrates excellent robustness when handling images with low SNR and sparse noise, while other methods fail to deliver satisfactory results.

Table IV renders the temporal expenditure of implementing all the unmixing methods. The simulations were conducted on MATLAB R2016a, utilizing a laptop equipped with an Intel Core i5-8300H CPU functioning at 2.30 GHz and 8 GB of RAM. The tests were performed on the simulated SDC2 dataset at an SNR of 20 dB. The findings indicate that the DRSU-TV algorithm took the most time to process as a result of its intricate model complexity, while the ADSpLRU, JSpBLRU, and RMSR algorithms were faster. RMSR was observed to be the fastest among the three algorithms. Although RMSR took longer time than

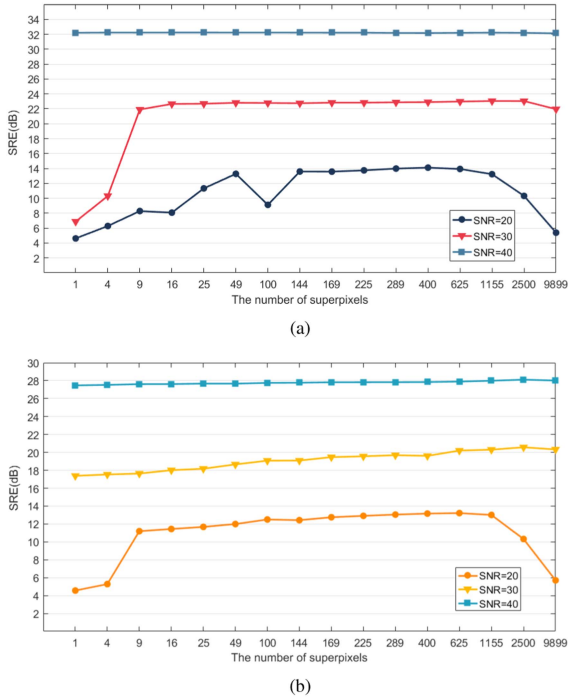


Fig. 11. SRE (dB) garnered through the propounded RMSR algorithm on SDC1 and SDC2 with different numbers of superpixels. (a) SDC1. (b) SDC2.

S^2 WSU and MUA algorithms due to its more comprehensive exploitation of spatial information from multiple perspectives, the time cost was still reasonable.

C. Analysis of Parameter Settings

Fig. 11(a) and (b) shows the trends of the SRE (dB) values and different numbers of superpixels obtained by the proposed RMSR algorithm on the simulated datasets SDC1 and SDC2 at different SNR levels. The results indicate that at an SNR of 20 dB, the unmixing outcome was considerably affected by the number of superpixels, resulting in suboptimal SRE (dB) values when the superpixels were partitioned into too many or too few blocks. For SDC1 with an SNR of 30 dB, the SRE (dB) curve tends to stabilize and reach the ideal results when the number of superpixels is greater than 16. For SDC2, the overall trend was that the SRE (dB) value increased as the number of superpixel blocks increased. The peak SRE (dB) value was obtained when the number of superpixel blocks was 2500. Under high SNR conditions, the number of superpixel blocks had little impact on the final unmixing result, and the overall trend was relatively stable.

We conducted two sets of simulated experiments to explore the selection of parameters to obtain the optimal SRE (dB) value. Fig. 12 shows the effects of regularization parameters λ and β on the unmixing performance of RMSR at an SNR of 20 dB. It indicates that the proposed algorithm can select λ and β in a relatively large range, which further demonstrates the effectiveness of the spatial and spectral weighting factors as well as the multiscale spatial regularization.

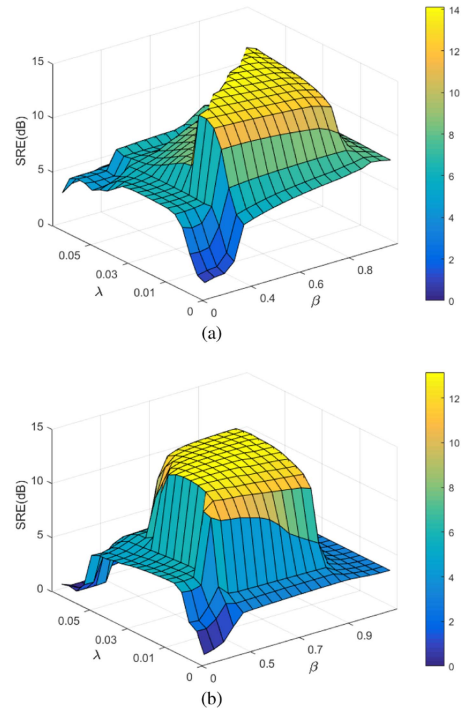


Fig. 12. SREs (dB) obtained by the proposed RMSR algorithm on (a) SDC1 and (b) SDC2 data with SNR of 20 dB, as functions of parameters λ and β .

IV. EXPERIMENTAL STUDY ON REAL HYPERSPECTRAL DATA

Within this division, we explicate empirical assays utilizing authentic documentation wherein the propounded RMSR method and comparative methods were leveraged on the Cuprite dataset and Mangrove dataset, respectively.

A. Cuprite Data

The experiment utilized the Cuprite dataset acquired in June 1997 by AVIRIS over the Cuprite region, Nevada, USA. The spectral reflectance values can be obtained online.² The dataset has 224 spectral channels, which span wavelengths from 0.4 to 2.5 μm and have a spectral resolution of 10 nm. Owing to the deficient SNR and pronounced water absorption, bands 1–2, 105–115, 150–170, and 223–224 were expunged, culminating in the utilization of 188 bands for the trial. A subset of the Cuprite data with 350×350 pixels was used in the experiment. The library $\mathbf{A}_1 \in \mathbb{R}^{188 \times 240}$ utilized in this experiment is identical to the one used in the SDC1 trial; however, the interference bands have been eliminated. Fig. 13 depicts the mineral geographical delineation constructed by USGS in 1995. The minerals were mapped using Tricorder 3.3 software [62].³ Note that the Tricorder mining area image was crafted in 1995, hence, it predates the cuprite datasets collection in 1997. So, the results of unmixing Cuprite dataset cannot be directly compared quantitatively with the map produced by the USGS, but the Fig. 13 can be used as a qualitative evaluation criterion.

²[Online] Available: <http://aviris.jpl.nasa.gov/html/aviris.freedata.html>.

³[Online] Available: <http://speclab.cr.usgs.gov/PAPER/tetracorder>.

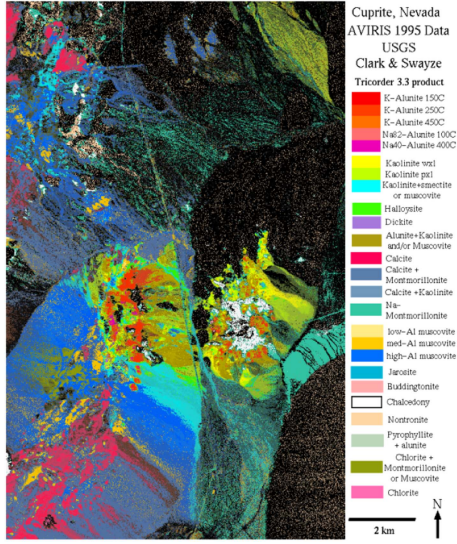


Fig. 13. Mineral map by USGS showing the mineral distribution within the Cuprite extractive precinct, Nevada.

Three minerals (Alunite, Buddingtonite, and Chalcedony) that are particularly prominent in the hyperspectral scene were selected to showcase their estimated abundance maps in Fig. 14. The regularization weights applied in ADSpLRU, JSpBLRU, DRSU-TV, MUA, S^2 WSU, and RMSR in this experiment were: $\lambda = 0.0005$ and $\tau = 0.001$, $\lambda = 0.05$ and $\tau = 0.2$, $\lambda = 0.002$ and $\lambda_{TV} = 0.0001$, $\lambda = 0.001$ and $\beta = 3$, $\lambda = 0.002$, as well as $\lambda = 0.001$ and $\beta = 0.5$, respectively. The figure demonstrates that all six algorithms can successfully analyze three types of minerals. The prognosticated abundance map engendered by the propounded RMSR algorithm exhibits superior verisimilitude to the referential taxonomic delineation synthesized by the Tricorder software, surpassing the other five methods. ADSpLRU, JSpBLRU, and MUA produced abundance maps for Buddingtonite with a significant amount of noise and Chalcedony abundance maps with varying degrees of information loss, showing significant difference from the reference images. The outcomes of DRSU-TV, S^2 WSU, and the propounded RMSR methods are relatively meritorious as they efficaciously delineate the dissemination of the three mineral constituents. The abundance map (Buddingtonite) obtained by RMSR stands out with significantly fewer noise, resulting in a cleaner map. Moreover, the sparsity of the results obtained by ADSpLRU, JSpBLRU, DRSU-TV, MUA, S^2 WSU, and RMSR is 0.0471, 0.0728, 0.0423, 0.0711, 0.0420, and 0.0407, respectively. It is evident that the RMSR algorithm has a lower sparsity compared with the other algorithms, indicating an advantage in sparse unmixing.

B. Mangrove Data

The data utilized in this experiment were acquired in October 2016 via an unmanned aerial vehicle equipped with the Cubert UHD185 hyperspectral imaging system, imaging the mangrove nature reserve on Qi'ao Island, Zhuhai City, China, with the specific area shown in Fig. 15(a) [63], [64]. The image

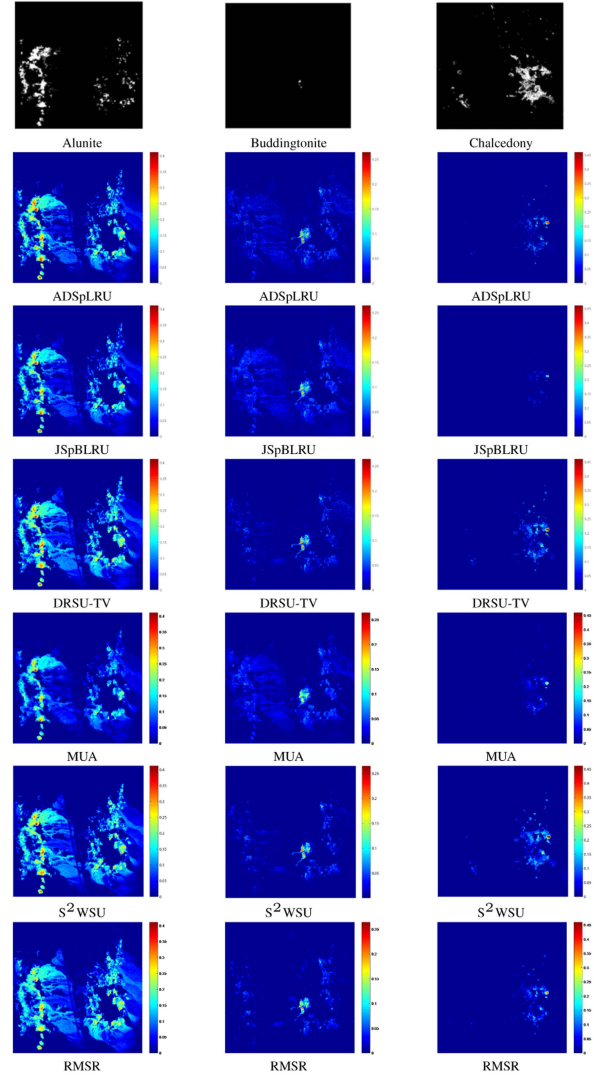


Fig. 14. Proportional abundance delineations prognosticated by ADSpLRU, JSpBLRU, DRSU-TV, MUA, S^2 WSU, and RMSR for the Cuprite subscene.

scene dimensions are 1878×1877 , with a wavelength range of 450–950 nm, a spectral resolution of 4 nm, and a total of 125 bands. The imagistic evidential data pervade approximately 3 hectares of mangrove biomes, and subsequent to antecedent processing the pictorials were resampled to a spatial discrimination of 0.02 m.

The predominant mangrove species found in the study area, as documented in [63] and [64], are *Kandelia candel* (KC), *Acanthus aureum* (AA), *Aegiceras corniculatum* (AC), *Sonneratia apetala* (SA), *Acanthus ilicifolius* (AI), and *Hymenocallis littoralis* (HL) & *Thespesia populnea* (TP). Other vegetation types, such as *Phragmites australis* (PA), tidal creeks, and wooden walkways, are also distributed in the region. It is worth noting that the imagery contains some shaded areas, which are also treated as a class of endmembers, owing to the presence of shadows in the image. The endmember spectral library $\mathbf{A}_3 \in \mathbb{R}^{125 \times 23}$, identical to those used in [65] and [66], is utilized in this study. Fig. 15(b) illustrates the spectral signatures for the seven major vegetation species contained in library \mathbf{A}_3 . The spectral

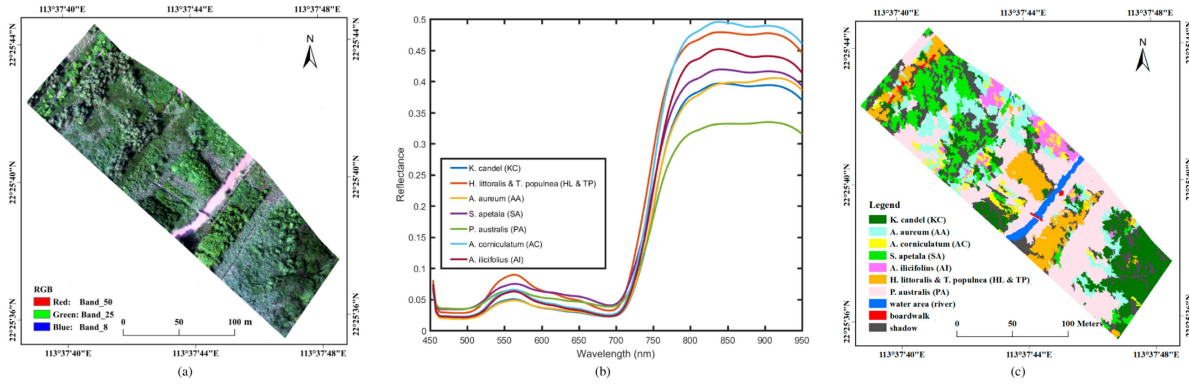


Fig. 15. Mangrove hyperspectral data. (a) UHD185 hyperspectral image. (b) Spectral reflectance profiles of seven vegetation species. (c) Classification map of UHD185 hyperspectral image.

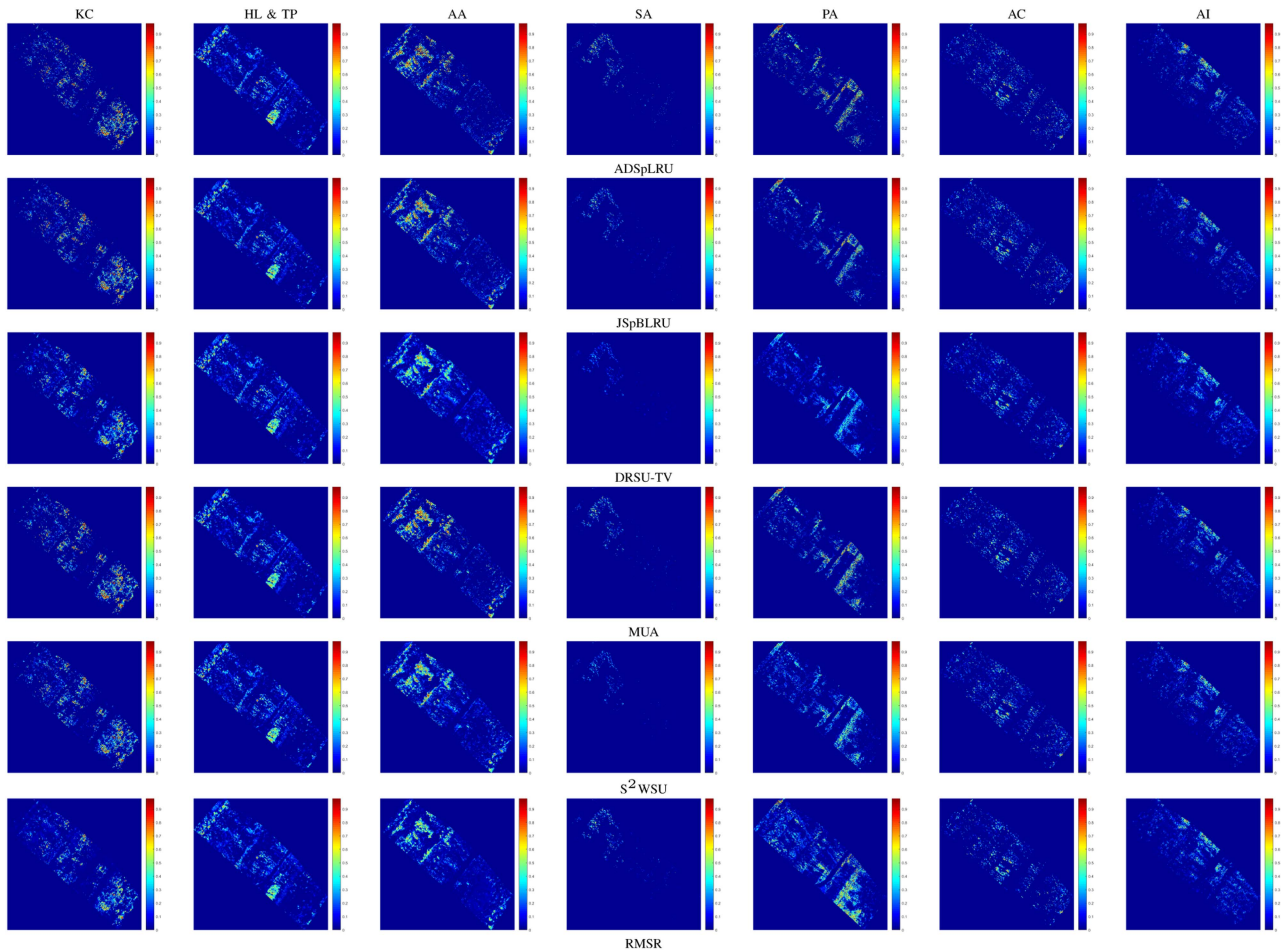


Fig. 16. Applying multiple sparse unmixing algorithms to the mangrove data produced abundance maps for seven characteristic mangrove vegetation types.

signatures in the figure exhibit a high degree of similarity across the various vegetation classes, presenting substantial challenges for spectral unmixing. For this study, we conduct a qualitative evaluation of the unmixing performance of various algorithms on the mangrove hyperspectral data by examining a mangrove species classification map [Referring to Fig. 15(c)] of our study area from Cao et al. [63], who utilized support vector machine classification.

In this experiment, the regularization parameters for the four examined algorithms—ADSpLRU, JSpBLRU, DRSU-TV, and S^2WSU —are selected based on recommendations from previous works [65] and [66]. Whereas the related regularization parameters for the MUA and RMSR algorithms are empirically set to $\lambda = 0.1$, $\beta = 50$, and $\lambda = 0.0001$, $\beta = 9$, respectively. The abundance maps for seven representative mangrove species—KC, HL&TP, AA, SA, PA, AC, and AI—derived by unmixing

this dataset using the examined algorithms are illustrated in Fig. 16. The regions in the figure where pixel abundance exceeds 0 denote the existence of the respective vegetation species. Fig. 16 demonstrates that the abundance maps produced by the six sparse unmixing methods show considerable agreement with the reference classification in multiple areas. This substantiates the capability of sparse unmixing techniques to effectively discriminate between the various endmembers present in the mangrove dataset. While the unmixing results of the algorithms cannot be quantitatively gauged, inspection of the figure reveals that the abundance maps derived by the proposed RMSR approach exhibit greater congruence with the reference classification for all endmembers. This signifies enhanced capacity of RMSR to represent the distributions of varied vegetation and preserve finer grained specifics (such as for PA species).

V. CONCLUSION

In this study, we proposed a robust and accurate sparse unmixing method, called RMSR, which introduced multiscale spectral–spatial regularization to integrate global spectral information, as well as irregular superpixel-based and regular neighborhood-based spatial information. A superpixel-guided spatial regularization term is proposed to alleviate the impact of noise on endmember identification. It constrains the discrepancy between the coarse abundance at the superpixel level and the estimated abundance of the original image using the $\ell_{2,1}$ norm. In addition, a spectral–spatial weighted sparse regularization term is introduced to constrain the number of active endmembers and the spatial correlation among neighboring pixels in the abundance map. Experimental results confirm the effectiveness of the combined multiscale spectral–spatial regularization in combating noise contamination and enhancing ground object separation performance. Highly mixed pixels existing in the edge regions of images is a challenge in hyperspectral unmixing. While the proposed RMSR algorithm implements multiscale spatial regularization, it offers limited effectiveness in preserving information in the edge regions. In the future, we will explore more precise prior knowledge, such as spatial structures or fine spectral endmember information, to better handle complex and challenging scenarios.

REFERENCES

- [1] J. M. Bioucas-Dias et al., “Hyperspectral unmixing overview: Geometrical, statistical, and sparse regression-based approaches,” *IEEE J. Sel. Topics Appl. Earth Observ. Remote Sens.*, vol. 5, no. 2, pp. 354–379, Apr. 2012.
- [2] J. M. Bioucas-Dias, A. Plaza, G. Camps-Valls, P. Scheunders, N. Nasrabadi, and J. Chanussot, “Hyperspectral remote sensing data analysis and future challenges,” *IEEE Geosci. Remote Sens. Mag.*, vol. 1, no. 2, pp. 6–36, Jun. 2013.
- [3] R. A. Borsoi et al., “Spectral variability in hyperspectral data unmixing: A comprehensive review,” *IEEE Geosci. Remote Sens. Mag.*, vol. 9, no. 4, pp. 223–270, Dec. 2021.
- [4] J. Li, J. M. Bioucas-Dias, A. Plaza, and L. Liu, “Robust collaborative nonnegative matrix factorization for hyperspectral unmixing,” *IEEE Trans. Geosci. Remote Sens.*, vol. 54, no. 10, pp. 6076–6090, Oct. 2016.
- [5] K. Atiya, D. V. Amol, M. Shankar, and C. H. Patil, “A systematic review on hyperspectral imaging technology with a machine and deep learning methodology for agricultural applications,” *Ecological Inform.*, vol. 69, 2022, Art. no. 101678.
- [6] M. Sergio et al., “Continental-scale hyperspectral tree species classification in the United States national ecological observatory network,” *Remote Sens. Environ.*, vol. 282, 2022, Art. no. 113264.
- [7] I. Dumke et al., “Underwater hyperspectral imaging using a stationary platform in the Trans-Atlantic geotraverse hydrothermal field,” *IEEE Trans. Geosci. Remote Sens.*, vol. 57, no. 5, pp. 2947–2962, May 2019.
- [8] M. Shimoni, R. Haelterman, and C. Perneel, “Hyperspectral imaging for military and security applications: Combining myriad processing and sensing techniques,” *IEEE Geosci. Remote Sens. Mag.*, vol. 7, no. 2, pp. 101–117, Jun. 2019.
- [9] B. Tu, X. Yang, W. He, J. Li, and A. Plaza, “Hyperspectral anomaly detection using reconstruction fusion of quaternion frequency domain analysis,” *IEEE Trans. Neural Netw. Learn. Syst.*, early access, Jan. 31, 2023, doi: [10.1109/TNNLS.2022.3227167](https://doi.org/10.1109/TNNLS.2022.3227167).
- [10] N. Keshava and J. F. Mustard, “Spectral unmixing,” *IEEE Signal Process. Mag.*, vol. 19, no. 1, pp. 44–57, Jan. 2002.
- [11] P. Ghamisi et al., “Advances in hyperspectral image and signal processing: A comprehensive overview of the state of the art,” *IEEE Geosci. Remote Sens. Mag.*, vol. 5, no. 4, pp. 37–78, Dec. 2017.
- [12] D. Hong et al., “Endmember-guided unmixing network (EGU-Net): A general deep learning framework for self-supervised hyperspectral unmixing,” *IEEE Trans. Neural Netw. Learn. Syst.*, vol. 33, no. 11, pp. 6518–6531, Nov. 2022.
- [13] W. K. Ma et al., “A signal processing perspective on hyperspectral unmixing: Insights from remote sensing,” *IEEE Signal Process. Mag.*, vol. 31, no. 1, pp. 67–81, Jan. 2014.
- [14] X. Xu, J. Li, C. Wu, and A. Plaza, “Regional clustering-based spatial pre-processing for hyperspectral unmixing,” *Remote Sens. Environ.*, vol. 204, pp. 333–346, 2018.
- [15] D. Hong, N. Yokoya, J. Chanussot, and X. X. Zhu, “An augmented linear mixing model to address spectral variability for hyperspectral unmixing,” *IEEE Trans. Image Process.*, vol. 28, no. 4, pp. 1923–1938, Apr. 2019.
- [16] M. E. Winter, “N-FINDR: An algorithm for fast autonomous spectral end-member determination in hyperspectral data,” *Proc. SPIE*, vol. 3753, pp. 266–275, 1999.
- [17] J. M. P. Nascimento and J. M. B. Dias, “Vertex component analysis: A fast algorithm to unmix hyperspectral data,” *IEEE Trans. Geosci. Remote Sens.*, vol. 43, no. 4, pp. 898–910, Apr. 2005.
- [18] S. Zhang, A. Agathos, and J. Li, “Robust minimum volume simplex analysis for hyperspectral unmixing,” *IEEE Trans. Geosci. Remote Sens.*, vol. 55, no. 11, pp. 6431–6439, Nov. 2017.
- [19] M. Berman, H. Kiveri, R. Lagerstrom, A. Ernst, R. Dunne, and J. F. Huntington, “ICE: A statistical approach to identifying endmembers in hyperspectral images,” *IEEE Trans. Geosci. Remote Sens.*, vol. 42, no. 10, pp. 2085–2095, Oct. 2004.
- [20] F. Schmidt, A. Schmidt, E. Treguier, M. Guiheneuf, S. Moussaoui, and N. Dobigeon, “Implementation strategies for hyperspectral unmixing using Bayesian source separation,” *IEEE Trans. Geosci. Remote Sens.*, vol. 48, no. 11, pp. 4003–4013, Nov. 2010.
- [21] H. Liu, Y. Lu, Z. Wu, Q. Du, J. Chanussot, and Z. Wei, “Bayesian unmixing of hyperspectral image sequence with composite priors for abundance and endmember variability,” *IEEE Trans. Geosci. Remote Sens.*, vol. 60, 2022, Art. no. 5503515.
- [22] W. He, H. Zhang, and L. Zhang, “Total variation regularized reweighted sparse nonnegative matrix factorization for hyperspectral unmixing,” *IEEE Trans. Geosci. Remote Sens.*, vol. 55, no. 7, pp. 3909–3921, Jul. 2017.
- [23] S. Zhang et al., “Spectral-spatial hyperspectral unmixing using nonnegative matrix factorization,” *IEEE Trans. Geosci. Remote Sens.*, vol. 60, 2022, Art. no. 5505713.
- [24] X.-R. Feng, H.-C. Li, R. Wang, Q. Du, X. Jia, and A. Plaza, “Hyperspectral unmixing based on nonnegative matrix factorization: A comprehensive review,” *IEEE J. Sel. Topics Appl. Earth Observ. Remote Sens.*, vol. 15, pp. 4414–4436, May 2022.
- [25] J. Li, A. Agathos, D. Zaharie, J. M. Bioucas-Dias, A. Plaza, and X. Li, “Minimum volume simplex analysis: A fast algorithm for linear hyperspectral unmixing,” *IEEE Trans. Geosci. Remote Sens.*, vol. 53, no. 9, pp. 5067–5082, Sep. 2015.
- [26] J. M. P. Nascimento and J. M. Bioucas-Dias, “Does independent component analysis play a role in unmixing hyperspectral data?,” *IEEE Trans. Geosci. Remote Sens.*, vol. 43, no. 1, pp. 175–187, Jan. 2005.
- [27] B. Yang, B. Wang, and Z. Wu, “Nonlinear hyperspectral unmixing based on geometric characteristics of bilinear mixture models,” *IEEE Trans. Geosci. Remote Sens.*, vol. 56, no. 2, pp. 694–714, Feb. 2018.

- [28] M. Elad, M. A. T. Figueiredo, and Y. Ma, "On the role of sparse and redundant representations in image processing," *Proc. IEEE*, vol. 98, no. 6, pp. 972–982, Jun. 2010.
- [29] K. M. Susan, J. H. Simon, A. R. Dar, and A. A. Elsa, "The ecostress spectral library version 1.0," *Remote Sens. Environ.*, vol. 230, 2019, Art. no. 111196.
- [30] M. D. Iordache, J. M. Bioucas-Dias, and A. Plaza, "Sparse unmixing of hyperspectral data," *IEEE Trans. Geosci. Remote Sens.*, vol. 49, no. 6, pp. 2014–2039, Jun. 2011.
- [31] S. Zhang, J. Li, K. Liu, C. Deng, L. Liu, and A. Plaza, "Hyperspectral unmixing based on local collaborative sparse regression," *IEEE Geosci. Remote Sens. Lett.*, vol. 13, no. 5, pp. 631–635, May 2016.
- [32] Z. Shi, T. Shi, M. Zhou, and X. Xu, "Collaborative sparse hyperspectral unmixing using l_0 norm," *IEEE Trans. Geosci. Remote Sens.*, vol. 56, no. 9, pp. 5495–5508, Sep. 2018.
- [33] M. D. Iordache, J. M. Bioucas-Dias, and A. Plaza, "Collaborative sparse regression for hyperspectral unmixing," *IEEE Trans. Geosci. Remote Sens.*, vol. 52, no. 1, pp. 341–354, Jan. 2014.
- [34] F. Chen and Y. Zhang, "Sparse hyperspectral unmixing based on constrained $l_p - l_2$ optimization," *IEEE Geosci. Remote Sens. Lett.*, vol. 10, no. 5, pp. 1142–1146, Sep. 2013.
- [35] E. J. Candès, M. B. Wakin, and S. P. Boyd, "Enhancing sparsity by reweighted l_1 minimization," *J. Fourier Anal. Appl.*, vol. 14, no. 5, pp. 877–905, 2008.
- [36] C. Y. Zheng, H. Li, Q. Wang, and C. L. P. Chen, "Reweighted sparse regression for hyperspectral unmixing," *IEEE Trans. Geosci. Remote Sens.*, vol. 54, no. 1, pp. 479–488, Jan. 2016.
- [37] R. Wang, H. C. Li, W. Liao, and A. Pižurica, "Double reweighted sparse regression for hyperspectral unmixing," in *Proc. IEEE Int. Geosci. Remote Sens. Symp.*, 2016, pp. 6986–6989.
- [38] F. Li, S. Zhang, B. Liang, C. Deng, C. Xu, and S. Wang, "Hyperspectral sparse unmixing with spectral-spatial low-rank constraint," *IEEE J. Sel. Topics Appl. Earth Observ. Remote Sens.*, vol. 14, pp. 6119–6130, Jun. 2021.
- [39] C. Shi and L. Wang, "Incorporating spatial information in spectral unmixing: A review," *Remote Sens. Environ.*, vol. 149, pp. 70–87, 2014.
- [40] R. Wang, H.-C. Li, W. Liao, X. Huang, and W. Philips, "Centralized collaborative sparse unmixing for hyperspectral images," *IEEE J. Sel. Topics Appl. Earth Observ. Remote Sens.*, vol. 10, no. 5, pp. 1949–1962, May 2017.
- [41] B. Tu, Q. Ren, Q. Li, W. He, and W. He, "Hyperspectral image classification using a superpixel-pixel-subpixel multilevel network," *IEEE Trans. Instrum. Meas.*, vol. 72, pp. 1–16, May 2023.
- [42] X. Xu, J. Li, S. Li, and A. Plaza, "Curvelet transform domain-based sparse nonnegative matrix factorization for hyperspectral unmixing," *IEEE J. Sel. Topics Appl. Earth Observ. Remote Sens.*, vol. 13, pp. 4908–4924, Aug. 2020.
- [43] M. D. Iordache, J. M. Bioucas-Dias, and A. Plaza, "Total variation spatial regularization for sparse hyperspectral unmixing," *IEEE Trans. Geosci. Remote Sens.*, vol. 50, no. 11, pp. 4484–4502, Nov. 2012.
- [44] R. Wang, H.-C. Li, A. Pižurica, J. Li, A. Plaza, and W. J. Emery, "Hyperspectral unmixing using double reweighted sparse regression and total variation," *IEEE Geosci. Remote Sens. Lett.*, vol. 14, no. 7, pp. 1146–1150, Jul. 2017.
- [45] R. Achanta, A. Shaji, K. Smith, A. Lucchi, P. Fua, and S. Süsstrunk, "SLIC superpixels compared to state-of-the-art superpixel methods," *IEEE Trans. Pattern Anal. Mach. Intell.*, vol. 34, no. 11, pp. 2274–2282, Nov. 2012.
- [46] T. Ince, "Superpixel-based graph Laplacian regularization for sparse hyperspectral unmixing," *IEEE Geosci. Remote Sens. Lett.*, vol. 19, 2022, Art. no. 5501305.
- [47] Z. Li, J. Chen, M. M. Movania, and S. Rahardja, "GPU implementation of graph-regularized sparse unmixing with superpixel structures," *IEEE J. Sel. Topics Appl. Earth Observ. Remote Sens.*, vol. 16, pp. 3378–3389, Mar. 2023.
- [48] X. Yang, B. Tu, Q. Li, J. Li, and A. Plaza, "Graph evolution-based vertex extraction for hyperspectral anomaly detection," *IEEE Trans. Neural Netw. Learn. Syst.*, early access, Aug. 25, 2023, doi: [10.1109/TNNLS.2023.3303273](https://doi.org/10.1109/TNNLS.2023.3303273).
- [49] R. Feng, Y. Zhong, and L. Zhang, "An improved nonlocal sparse unmixing algorithm for hyperspectral imagery," *IEEE Geosci. Remote Sens. Lett.*, vol. 12, no. 4, pp. 915–919, Apr. 2015.
- [50] R. A. Borsoi, T. Imbiriba, J. C. M. Bermudez, and C. Richard, "A fast multiscale spatial regularization for sparse hyperspectral unmixing," *IEEE Geosci. Remote Sens. Lett.*, vol. 16, no. 4, pp. 598–602, Apr. 2019.
- [51] S. Zhang, J. Li, H. Li, C. Deng, and A. Plaza, "Spectral-spatial weighted sparse regression for hyperspectral image unmixing," *IEEE Trans. Geosci. Remote Sens.*, vol. 56, no. 6, pp. 3265–3276, Jun. 2018.
- [52] H.-C. Li, X.-R. Feng, D.-H. Zhai, Q. Du, and A. Plaza, "Self-supervised robust deep matrix factorization for hyperspectral unmixing," *IEEE Trans. Geosci. Remote Sens.*, vol. 60, pp. 1–14, 2022, Art. no. 5513214.
- [53] C. Deng et al., "Robust dual spatial weighted sparse unmixing for remotely sensed hyperspectral imagery," *Remote Sens.*, vol. 15, no. 16, Aug. 2023, Art. no. 4056.
- [54] L. Dong, X. Lu, G. Liu, and Y. Yuan, "A novel NMF guided for hyperspectral unmixing from incomplete and noisy data," *IEEE Trans. Geosci. Remote Sens.*, vol. 60, pp. 1–15, 2022, Art. no. 5513515.
- [55] E. J. Candès and T. Tao, "Near-optimal signal recovery from random projections: Universal encoding strategies?," *IEEE Trans. Inf. Theory*, vol. 52, no. 12, pp. 5406–5425, Dec. 2006.
- [56] S. S. Chen and D. Saunders, "Atomic decomposition by basis pursuit," *SIAM Rev.*, vol. 43, no. 1, pp. 129–159, 2001.
- [57] J. M. Bioucas-Dias and M. A. T. Figueiredo, "Alternating direction algorithms for constrained sparse regression: Application to hyperspectral unmixing," in *Proc. IEEE 2nd Workshop Hyperspectral Image Signal Process. Evol. Remote Sens.*, 2010, pp. 1–4.
- [58] X. Wang, Y. Zhong, L. Zhang, and Y. Xu, "Spatial group sparsity regularized nonnegative matrix factorization for hyperspectral unmixing," *IEEE Trans. Geosci. Remote Sens.*, vol. 55, no. 11, pp. 6287–6304, Nov. 2017.
- [59] P. V. Giampouras, K. E. Themelis, A. A. Rontogiannis, and K. D. Koutroumbas, "Simultaneously sparse and low-rank abundance matrix estimation for hyperspectral image unmixing," *IEEE Trans. Geosci. Remote Sens.*, vol. 54, no. 8, pp. 4775–4789, Aug. 2016.
- [60] J. Huang, T. Z. Huang, L. J. Deng, and X. -L. Zhao, "Joint-sparse-blocks and low-rank representation for hyperspectral unmixing," *IEEE Trans. Geosci. Remote Sens.*, vol. 57, no. 4, pp. 2419–2438, Apr. 2019.
- [61] G. Martin and A. Plaza, "Spatial-spectral preprocessing prior to endmember identification and unmixing of remotely sensed hyperspectral data," *IEEE J. Sel. Topics Appl. Earth Observ. Remote Sens.*, vol. 5, no. 2, pp. 380–395, Apr. 2012.
- [62] R. Clark et al., "Imaging spectroscopy: Earth and planetary remote sensing with the USGS tetraorder and expert systems," *J. Geophys. Res.*, vol. 108, no. E12, pp. 5131–5135, Dec. 2003.
- [63] J. Cao, W. Leng, K. Liu, L. Liu, Z. He, and Y. Zhu, "Object-based mangrove species classification using unmanned aerial vehicle hyperspectral images and digital surface models," *Remote Sens.*, vol. 10, no. 1, 2018, Art. no. 89.
- [64] J. Cao, K. Liu, L. Liu, Y. Zhu, J. Li, and Z. He, "Identifying mangrove species using field close-range snapshot hyperspectral imaging and machine-learning techniques," *Remote Sens.*, vol. 10, no. 12, 2018, Art. no. 2047.
- [65] F. Li, S. Zhang, C. Deng, B. Liang, J. Cao, and S. Wang, "Robust double spatial regularization sparse hyperspectral unmixing," *IEEE J. Sel. Topics Appl. Earth Observ. Remote Sens.*, vol. 14, pp. 12569–12582, Dec. 2021.
- [66] F. Li et al., "Sparse unmixing with truncated weighted nuclear norm for hyperspectral data," *Nat. Remote Sens. Bull.*, vol. 26, no. 6, pp. 1067–1082, 2022.



Ke Wang received the B.S. degree in automation from East China Jiaotong University, Nanchang, China, in 2018, and the M.S. degree in electrical engineering from Washington State University, Pullman, WA, USA, in 2022.

He is currently a Visiting Student with the School of Computer Science, China University of Geosciences, Wuhan, China. His major research interests include blind source separation and signal processing.



Lei Zhong received the B.S. degree in geographic information systems from Hunan Normal University, Changsha, China, in 2004.

He is currently an Engineer with the Third Surveying and Mapping Institute of Hunan Province, Changsha. His research interests include basic surveying and aerial photogrammetry, as well as image processing analysis.



Jiajun Zheng received the B.S. degree in information management and information system in 2022 from the Nanchang Institute of Technology, Nanchang, China, where he is currently working toward the M.E. degree in electronic information with the School of Information Engineering.

His current research interests include hyperspectral image processing and signal processing.



Chengzhi Deng received the B.S. degree in communication engineering and the M.S. degree in optics from Jiangxi Normal University, Nanchang, China, in 2002 and 2005, respectively, and the Ph.D. degree in information and communication engineering from the Huazhong University of Science and Technology, Wuhan, China, in 2008.

He is currently a Professor with the School of Information Engineering, Nanchang Institute of Technology, Nanchang. His research interests include hyperspectral image processing and machine learning.



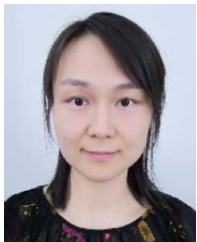
Shaoquan Zhang (Member, IEEE) received the B.S. degree in communication engineering and the M.E. degree in power engineering from the Nanchang Institute of Technology, Nanchang, China, in 2012 and 2015, respectively, and the Ph.D. degree in cartography and geography information system from Sun Yat-sen University, Guangzhou, China, in 2018.

He is currently a Distinguished Professor with the School of Information Engineering, Nanchang Institute of Technology. His research interests include hyperspectral unmixing and deep learning.



Jingjing Cao received the B.S. degree in geographic information system from Xinyang Normal University, Xinyang, China, in 2011, and the M.S. and Ph.D. degrees in cartography and geographic information system from Sun Yat-sen University, Guangzhou, China, in 2013 and 2019, respectively.

She is currently a Lecturer with the College of Computer Sciences, Guangdong Polytechnic Normal University, Guangzhou. Her current research interests include vegetation remote sensing and urban remote sensing.



Fan Li received the B.S. degree in computer science and technology from Wuhan University, Wuhan, China, in 2004, and the M.E. degree in computer technology from Jiangxi Normal University, Nanchang, China, in 2020. She is currently working toward the Ph.D. degree in geoinformation engineering with the School of Computer Science, China University of Geosciences, Wuhan.

She is also an Associate Professor with the School of Information Engineering, Nanchang Institute of Technology, Nanchang. Her research interests include hyperspectral unmixing and image fusion.



Dingli Su received the B.S. degree in mechanics and the Ph.D. degree in engineering mechanics from Sun Yat-sen University, Guangzhou, China, in 2013 and 2018, respectively.

He is currently a Senior Engineer with the Guangzhou Institute of Building Science Group Co., Ltd., Guangzhou. His research interests include geotechnical exploration and application analysis and image processing.